Article

Establishing the Link across the Synthesis Reaction Kinetics, Structural Changes, and Photocatalytic Efficiency of an Enhanced Chitosan–Clay (1:3) Nanocomposite

Wael Albouchi [†], Malek Lahbib [†], Chadha Mejri [ID], Sana Jebali, Mahdi Meftah and Walid Oueslati *[ID]

LR19ES20: Resources, Materials and Ecosystems (RME), Faculty of Sciences of Bizerte, University of Carthage, Bizerte 7021, Tunisia; meftahmahdi@yahoo.fr (M.M.)
* Correspondence: walidoueslati@ymail.com
[†] These authors contributed equally to this work.

Abstract: This research investigates the influence of synthesis kinetics on the structural and photocatalytic properties of chitosan–clay nanocomposites (Cs/MMT) and chitosan–hectorite nanocomposites (Cs/HET), employing an optimized initial stoichiometry of 1:3. Utilizing a variety of analytical techniques, including X-ray diffraction (XRD), transmission electron microscopy (TEM), and Fourier-transform infrared spectroscopy (FTIR), the study explores the structural evolution of the nanocomposites and their photocatalytic performance using semiconductor catalysts TiO_2 and ZnO. The findings emphasize the significant impact of reaction kinetics, particularly after 3 h of reaction time, on the structural features of the nanocomposites. Notably, Cs/MMT demonstrates greater crystalline stability compared to Cs/HET due to variations in octahedral cavity occupancy in the initial clays. FTIR and TEM analyses depict the progressive evolution of the nanocomposites during the reaction, shedding light on how reaction kinetics drive the formation of specific bonds within the nanocomposites. In terms of photocatalytic activity, this study provides insights into the complex dynamics of photocatalytic degradation, with a specific focus on the performance of TiO_2 and ZnO under diverse experimental conditions. The superior efficacy of TiO_2 as a catalyst, particularly when integrated with Cs/MMT nanocomposites, is unequivocally demonstrated, with degradation rates exceeding 80%. This preference stems from TiO_2 consistently exhibiting higher degradation rates compared to ZnO, attributed to structural disparities between montmorillonite and hectorite, influencing catalyst–support interactions. The findings underscore the critical importance of selecting suitable catalyst and support matrix combinations for optimizing performance in specific applications.

Keywords: hybrid materials; chitosan–clay nanocomposite; structural features; photocatalytic activity; reaction time; Cibacron Brilliant Yellow 3GP dye

1. Introduction

The rapid development of the textile sector has led to a significant challenge in many countries: the accumulation of organic pollutants, particularly dyes, in wastewater. Due to their chemical stability and slow biodegradation in the environment, these organic compounds pose a potential threat to the local ecosystem. To prevent the discharge of untreated wastewater containing these toxins into aquatic environments, efficient and cost-effective treatment methods are crucial.

Advanced oxidation processes (AOPs) are a promising technology for wastewater treatment. AOPs are being increasingly used to reduce the amount of organic pollutants in various wastewater streams from different industrial sites [1–4]. Among these AOPs, heterogeneous photocatalysis has demonstrated high effectiveness in breaking down resistant organic molecules and transforming them into readily biodegradable compounds [5–8].

Heterogeneous photocatalysis is a powerful and versatile environmental remediation technique that leverages semiconductor materials to accelerate chemical reactions when

exposed to light. This process excels at breaking down a broad spectrum of resistant organic molecules.

One of the key advantages of heterogeneous photocatalysis is its ability to tackle persistent organic pollutants (POPs) and other stubborn contaminants present in water and air. By harnessing the energy of photons (light particles), photocatalysts generate electron–hole pairs that trigger redox reactions. These reactions degrade complex organic compounds into simpler, less harmful substances. This process is particularly effective for treating challenging pollutants like pesticides, pharmaceutical residues, and industrial dyes, which often prove difficult to remove using conventional methods.

Despite its strengths, implementing heterogeneous photocatalysis comes with some challenges. The effectiveness of this process hinges heavily on choosing the right semiconductor material, designing the catalyst effectively, and optimizing reaction conditions [9–11].

Among semiconductor metal oxides, titanium dioxide (TiO_2) reigns supreme as the most widely used photocatalyst for organic molecule degradation. However, it possesses a relatively high bandgap energy (3.2 eV), limiting its light absorption to ultraviolet light. Similarly, zinc oxide (ZnO) has become a popular and cost-effective alternative due to its decent photoactivity and a bandgap energy comparable to TiO_2 [5,12,13].

A groundbreaking development in photocatalysis research is the emergence of nanocomposite materials, which offer a new approach to environmental cleanup and pollutant degradation. These innovative materials integrate nanoscale structures, often combining multiple materials or phases, to enhance catalytic activity and absorb a wider range of light. The unique properties of nanocomposites allow them to outperform their individual components. This breakthrough opens doors for utilizing renewable energy sources and eliminating persistent organic pollutants more effectively. By meticulously designing and synthesizing nanocomposite photocatalysts, researchers see immense potential for significantly increasing the efficiency and practicality of photocatalytic processes [14–25].

Natural biopolymer chitosan and clay minerals have been innovatively combined in chitosan–clay nanocomposites. This novel substance possesses exceptional qualities as a result of its effective synthesis. Due to the presence of amino groups ($-NH_2$) and hydroxyl groups (-OH) acting as adsorption sites, chitosan is widely used in food preservation, cosmetic products, drug delivery systems, and wastewater treatment [5–7].

Clay adds increased mechanical strength and structural stability, while chitosan, which is made from chitin, offers biodegradability and biocompatibility. The resulting nanocomposite has enormous potential for use in a variety of fields, including biomedicine, environmental remediation, and other fields [15,26–33].

The enhanced surface contact between each component strengthens the interaction between the nanofillers and the polymer matrix. The nature of the reinforcement (nanofillers) and the type of polymer fraction establish different types of nanocomposites.

The effects of reactant ratio and type of nanofiller on the microstructural characteristics, porosity, and capability of heavy metal removal of chitosan–clay nanocomposites were explored in an earlier study by the same group of authors [32]. Dioctahedral and trioctahedral smectite clays are the two different nonfiller types used [34–37]. The outcomes show that the synthesis of the nanocomposite was effective. According to the research, a stoichiometry ratio of 1:3 promotes intercalation and increases crystallite size and crystallinity. Atomic absorption spectroscopy tests the nanocomposites' ability to adsorb Pb^{2+} and Cd^{2+} cations in solutions of slightly saturated soil, with extremely encouraging results for dioctahedral smectite.

In continuation of the earlier study [34], the focus has shifted towards investigating and optimizing the synthesis kinetics of the 1:3 sample stoichiometry. This endeavor aims to enhance the photocatalytic activity of the resulting nanocomposites. This strategic approach represents a crucial step forward in unlocking the full potential of these materials for advanced applications in environmental remediation. The goal is to delve into the underlying kinetics and subsequently elevate the photocatalytic capabilities of the synthesized nanocomposites. Indeed, while numerous research endeavors have explored chitosan–clay

nanocomposites [38–40], a critical aspect has remained largely unaddressed: the influence of octahedral cavity occupancy within the base sheet. Additionally, the synthesis kinetics and the potential for optimization towards an exceptionally efficient nanocomposite have seldom been examined, particularly within the context of serious consideration for its application as a photocatalyst. This represents an important gap in the existing body of study, as understanding and fine-tuning these parameters hold significant promise for advancing the field of nanocomposite technology.

2. Materials and Methods

2.1. Starting Reagents: Formula and Composition

2.1.1. Nanofillers

This study looks at how two different types of starting clays affect nanofiller structure. One clay, hectorite, has a tri-octahedral charge, while the other, montmorillonite, has a di-octahedral charge. Montmorillonite is called SWy-2 and comes from Wyoming, USA. Hectorite, known as SHCa-1, comes from San Bernardino, CA, USA. Its chemical composition (%): SiO_2: 34.7, Al_2O_3: 0.69, TiO_2: 0.038, Fe_2O_3: 0.02, FeO: 0.25, MnO: 0.008, MgO: 15.3, CaO: 23.4, Na_2O: 1.26, K_2O: 0.13, Li_2O: 2.18, F: 2.60, P_2O_5: 0.014, S: 0.01 [38]. Both clays mainly have Mg ions in their structure, but hectorite also has Li^+ ions. The formulas of montmorillonite and hectorite show their unique properties. Montmorillonite has layers and can swap ions, while hectorite has a trioctahedral structure. Its chemical composition (%): SiO_2: 62.9, Al_2O_3: 19.6, TiO_2: 0.090, Fe_2O_3: 3.35, FeO: 0.32, MnO: 0.006, MgO: 3.05, CaO: 1.68, Na_2O: 1.53, K_2O: 0.53, F: 0.111, P_2O_5: 0.049, S: 0.05 [38]. Before use, natural samples are treated with a NaCl solution to help them disperse evenly. The process for making montmorillonite or hectorite suspension follows a set method explained in references [34,39,40] and shown in Figure 1. The samples are named MMT-Na (montmorillonite) and HET-Na (hectorite).

2.1.2. Chitosan (Cs)

This study incorporates a class of linear polysaccharides, commercially known as Cs, which are produced by partially deacetylating chitin. This compound is derived from either the exoskeletons of crustaceans or the cell walls of fungi [41,42]. Cs manifests as copolymers consisting of -(1-4)-linked glucosamine and N-acetylglucosamine. The chitosan used in this study was provided by Glentham Life Sciences, based in Wiltshire, UK, with the CAS number 9012-76-4. Detailed specifications from the supplier are outlined in Table S1. Additionally, chemical reagents, including NaCl, NaOH, acetic acid, $PbCl_2$, and $CdCl_2$, were sourced from Merck in Germany. All supplementary chemicals, meeting analytical-grade standards, were also procured from Merck in Germany. Notably, all solutions were prepared using deionized water, ensuring high-quality standards for the experimental procedures.

2.2. Experimental Synthesis Process

The synthesis of Cs/HET and Cs/MMT nanocomposites followed a well-defined protocol. Precisely weighed amounts (0.25 g chitosan, 0.75 g each of MMT-Na and HET-Na) were used. The chitosan was dissolved in a 2% acetic acid solution and centrifuged. Meanwhile, the clay fraction was dispersed in 50 mL of distilled water. Subsequently, the clay suspension was added to the chitosan solution, and the mixture was stirred at 60 °C for 6 h. The resulting composite was then oven-dried at 60 °C for 48 h. Following this, the composite underwent a 5 h soaking step in a 1 M NaOH solution, followed by multiple rinses with distilled water. Finally, the composite was dried again in an oven at 60 °C for 48 h. This meticulous procedure ensured the successful synthesis of Cs/HET and Cs/MMT nanocomposites, paving the way for subsequent analyses and characterizations.
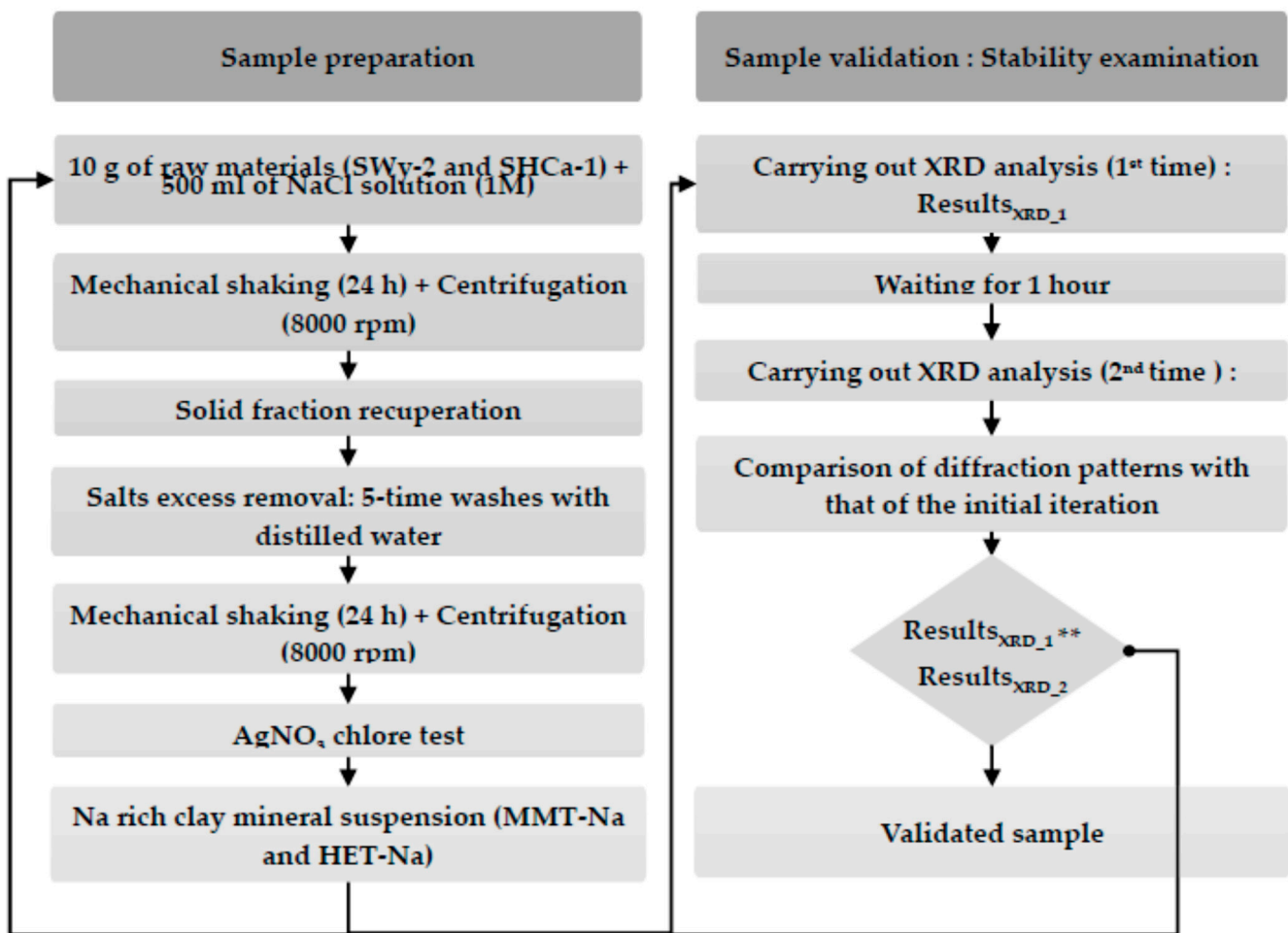
(**) Reproduction of the same diffraction pattern with slight variations.

Figure 1. Pretreatment of the cationic clays MMT-Na and HET-Na [43–47].

2.3. Controlling Reaction Kinetics for Enhanced Nanocomposite Synthesis

Understanding the reaction kinetics during the synthesis of Cs/MMT and Cs/HET nanocomposites is crucial for optimizing production methods [48]. The final structure and functionality of these hybrid nanocomposites are heavily influenced by the reaction time. To monitor the kinetic behavior, samples are extracted from the reaction mixture at hourly intervals. Five samples are collected at each time point: 1, 2, 3, 4, and 5 h after the start of the reaction, for each initial mixture. It is important to note that both starting mixtures maintain a constant 1:3 ratio of chitosan to clay (Cs/MMT or Cs/HET). This thorough methodology allows for an in-depth examination of how different reaction times affect the entire synthesis process. Ultimately, by understanding these details, we can tailor the production process to achieve the desired properties in the final nanocomposite.

2.4. Characterization Techniques
2.4.1. X-ray Diffraction Analysis (XRD)

A Bruker D8 ADVANCE X-ray diffractometer equipped with monochromatic Cu-Kα radiation (λ = 1.5406 nm) was used to examine the crystalline structures of the samples. The analysis was conducted at 40 kV and 20 mA. Standard scanning parameters included a step size of 0.01° in 2θ and a counting time of 6 s per step across the investigated angular range. XRD profiles were systematically recorded for all specimens within a 2θ range of 3° to 40° [28,37,39,49–52]. The Bragg relation was employed to determine the basal spacing value, while the Scherrer equation was used to calculate the average crystallite size. It

is important to note that all measurements were carried out at room temperature under atmospheric pressure [15,53–55].

2.4.2. Fourier Transform Infrared Spectroscopy (FTIR)

Thermo Nicolet's Avatar 370 FTIR spectrometer (Thermo Fisher Scientific., Schwerte, Germany), which has a KBr beam splitter and a DTGS detector, was used to obtain the FTIR spectrum. Data were gathered at a resolution of 4 cm^{-1} and over the wavelength range of 4000 to 400 cm^{-1} for each spectra using 56 scans.

2.4.3. TEM Scanning and Energy-Dispersive X-ray Spectroscopy (EDX)

Transmission electron microscopy (TEM) was employed to analyze the nanostructure and morphology of the powdered materials using a FEI Tecnai G2 (FEI, Eindhoven, Netherlands) operating at an acceleration voltage of 200 kV. To prepare TEM specimens, samples were first fractured and dispersed in ethanol. A drop of the resulting suspension was then deposited onto a holey carbon-coated copper grid. Local chemical analysis was performed using an energy-dispersive X-ray spectroscopy (EDX) system in conjunction with a Carl Zeiss Ultra 55 field-emission scanning electron microscope (SEM) (Carl Zeiss, Jena, Germany).

### 2.4.4. UV-Visible Spectroscopy

The Shimadzu UV-2600 spectrophotometer (Shimadzu Corporation, Kyoto, Japan) played a critical role in this investigation. This advanced equipment was employed to meticulously record both UV-visible diffuse reflectance and absorbance spectra for all samples across a broad spectral range of 200–400 nm. The high precision of the instrument ensured the acquisition of comprehensive data, facilitating a thorough analysis of the materials' optical properties within this crucial wavelength region. These insights proved invaluable in understanding the behavior of the materials under study.

2.4.5. Photocatalytic Application

The photocatalytic degradation method offers a promising approach for eliminating organic pollutants from wastewater. This technique utilizes semiconductor materials like titanium dioxide (TiO_2) and zinc oxide (ZnO) as supports for semiconductor particles with catalytic properties. In this study, we aim to improve our understanding of the Cibacron Brilliant Yellow 3GP dye degradation process by leveraging the photocatalytic properties of Cs/MMT and Cs/HET nanocomposites. These nanocomposites act as supports for the semiconductor particles, increasing the available surface area for dye adsorption and potentially leading to a synergistic effect and enhanced dispersion of the photocatalyst.

Cibacron Brilliant Yellow 3G-P ($C_{25}H_{15}Cl_3N_9Na_3O_{10}S_3$), obtained from Sigma-Aldrich (Merck KGaA, Darmstadt, Germany), possesses three sulfonate groups that become negatively charged in water. It exhibits an absorption peak at 404 nm, a color index value of 18,972, and a molecular weight of 831.02 g/mol. The stability of Cibacron Brilliant Yellow 3G-P, a synthetic product, is influenced by several factors. These factors encompass the light source, with UV light posing a greater risk of photodegradation compared to visible light. Furthermore, specific compounds like TiO and ZnO can exacerbate this degradation process, particularly in the presence of oxygen. Additionally, the pH level of the surrounding environment is pivotal, as acidic conditions can expedite the deterioration of the dye. Double-distilled water was used in all tests to eliminate impurities. NaOH (Sigma-Aldrich, Merck KGaA-Darmstadt, Germany) and nitric acid (TEDIA, Fairfield, OH, USA) were employed to adjust the pH to 5. All other chemicals, unless otherwise specified, were of analytical grade. The dye was utilized in its unpurified, as-received state [56–58].

For the experiment, a 2066 W, 230 V, 50–60 Hz UV lamp with a cooling water circuit served as the light source. The UV light was positioned 6.0 cm from the photoreactor. Figure 2 illustrates the photocatalytic reaction setup.
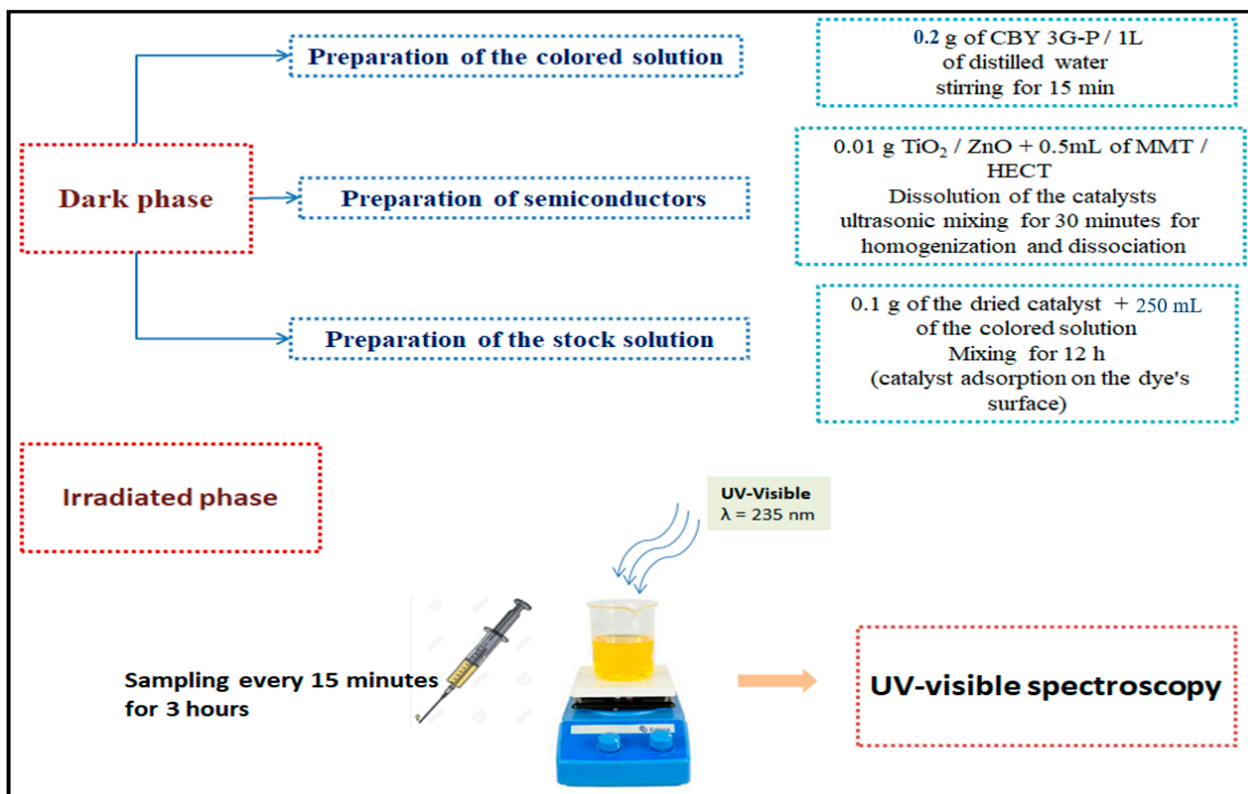
Figure 2. Experimental process for photocatalytic application.

The photocatalytic process is initiated by simultaneous exposure to ultraviolet (UV) light with a focused wavelength of 235 nm. To assess the method's efficacy, samples were collected at consistent 15 min intervals over a total duration of 180 min. This time series allows for the analysis of the degradation reaction's progress over time. Various factors are considered in this evaluation, including reaction kinetics, the type of semiconductor employed (TiO$_2$ or ZnO), and the octahedral occupation type of the initial nanofiller.

3. Results

3.1. XRD Analysis

XRD Study of the Structural Evolution of the Cs/MMT and Cs/HET Samples (1:3)

X-ray diffraction (XRD) analysis reveals intriguing differences in the structural evolution of Cs/MMT (1:3) and Cs/HET (1:3) samples.

Cs/MMT (1:3): After one hour of reaction (Figure 3), Cs/MMT exhibits a broad reflection at 21.82 Å, indicating an expansion of the interlamellar space due to chitosan intercalation. This is contrasted by Cs/HET, where the initial diffractogram lacks characteristic peaks, suggesting a near-complete exfoliation of hectorite layers. This difference highlights the varying reactivity of the clays—montmorillonite responds readily, while hectorite undergoes a slower, more progressive transformation.

Over time, Cs/MMT displays a dynamic interplay of reflections. The 15 Å and 12 Å peaks corresponding to hydrated interstratification fluctuate, likely due to variations in hydration and the formation of distinct layer populations. Conversely, Cs/HET exhibits a distinct reaction pattern (Figure 4). A single reflection at 16.76 Å emerges after two hours, indicative of an intermediate hydration state or the presence of chitosan within the layers. This slower reaction likely stems from differences in the clays' octahedral cavity occupancy.
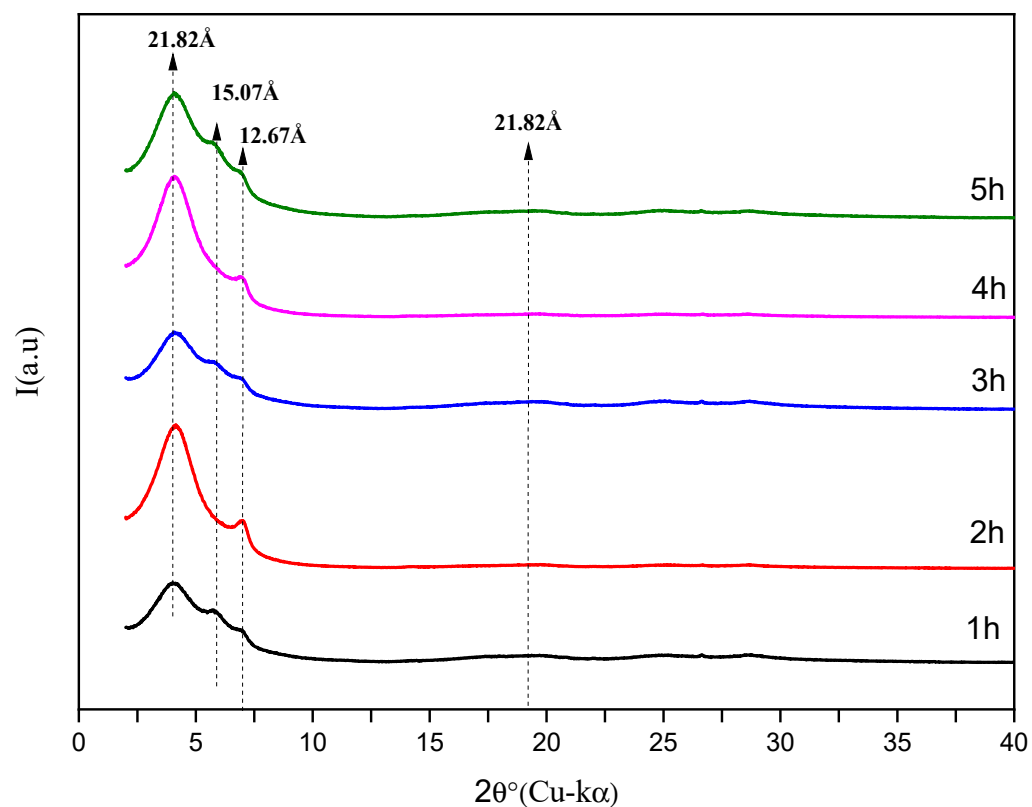
Figure 3. Evolution of experimental XRD profiles as a function of the reaction kinetics for the Cs/MMT (1:3) sample.
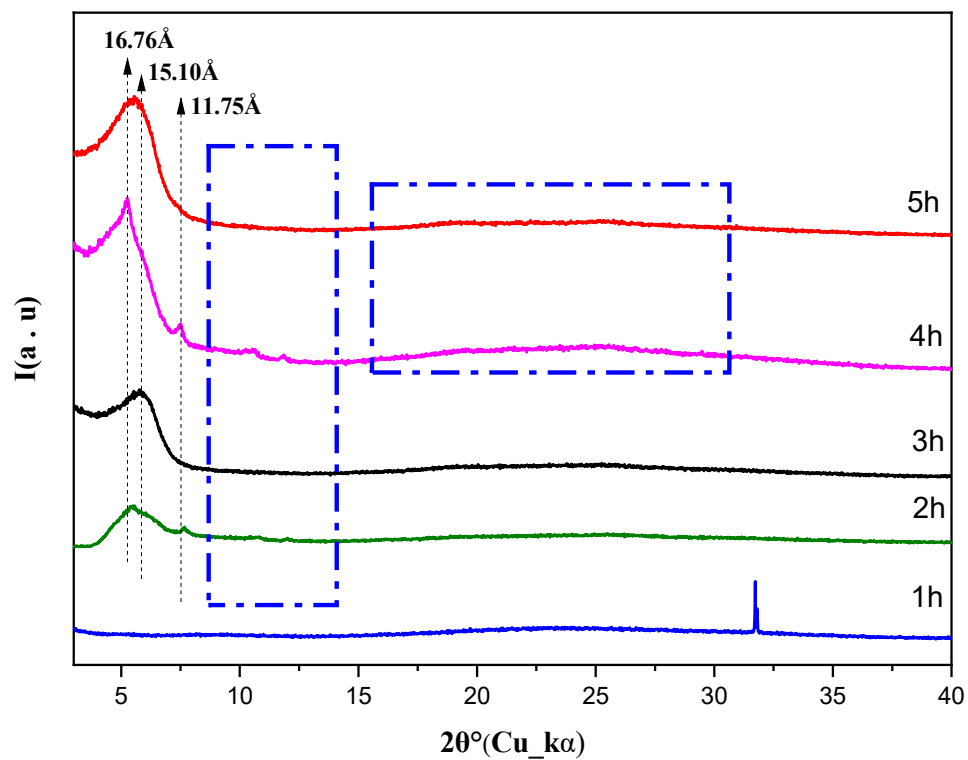
Figure 4. Evolution of experimental XRD profiles as a function of the reaction kinetics for the Cs/HET (1:3) sample.

Both samples ultimately reach a heterogeneous state, as evidenced by the emergence of chitosan reflections and the broadening of peaks (FWHM) in later stages. However, the contrasting reaction kinetics are undeniable. Cs/MMT undergoes a swifter structural reorganization due to its inherent reactivity, while Cs/HET exhibits a more gradual transformation. These findings emphasize the importance of clay type in dictating the final structure and properties of the synthesized nanocomposite [15,34,59–62].

Determining crystallite size is a pivotal procedure in characterizing the crystalline structure of materials, particularly in materials science. This parameter can be deduced from empirical data acquired through techniques like X-ray diffraction (XRD) or electron diffraction (TEM). The Scherrer method, a widely adopted approach, estimates crystallite size based on X-ray diffraction peaks. This estimation relies on Equation (1):

$$D = k\lambda / \beta \cos(\theta) \tag{1}$$

Indeed, the Scherrer method follows a systematic approach. First, it entails accurately measuring the full width at half maximum (FWHM) of the diffraction peak, denoted as β, from the experimental dataset. Subsequently, one needs to consider the wavelength of the X-rays (λ) used for the diffraction. Additionally, it is crucial to identify the specific diffraction angle (θ) corresponding to the peak under analysis. Once armed with these essential values, they are then inputted into the formula, culminating in the calculation of the crystallite size, represented as D. This methodological sequence is fundamental to extracting crucial insights about the crystalline structure of materials in the field of materials science. All calculated crystallite sizes are presented in Table 1.

Table 1. Calculation of crystallite size.

Samples	Time (h)	X-ray Wavelength λ (Å)	Diffraction Angle θ (°)	FWHM (rad)	Crystallite Size D (nm)
Cs/MMT	1		2.015	0.133	3.830
	2		2.045	0.116	2.129
	3		2.150	0.375	1.948
	4		2.112	0.373	1.698
	5		2.112	0.374	1.696
Cs/HET	1	1.5406 Å	*	*	**
	2		2.789	0.127	4.140
	3		2.634	0.593	3.847
	4		2.949	0.592	3.824
	5		2.789	0.591	3.559

Note: (*) denotes the absence of a peak, and (**) denotes complete exfoliation.

The crucial importance of crystallite size in optimized crafting and functional structures (intercalated or exfoliated) can be explained as follows:

When clay crystallites are of reduced dimensions, it significantly facilitates the polymer's intercalation between the clay layers. A smaller crystallite size provides more space and flexibility for the polymeric chains to fit between the layers, establishing tighter and more uniform bonds. This configuration promotes an optimal dispersion of the polymer within the clay matrix, creating an intercalated structure. Thanks to this specific arrangement, the properties and performance of the composite material are significantly enhanced. With increasing crystallite size, the challenge of polymer intercalation between the clay layers intensifies significantly. This dimensional increase restricts the available space for intercalation, making the process less straightforward. In this scenario, the clay layers are forced apart, resulting in an exfoliated structure. This transformation, offering a larger and more conducive space for polymer insertion, has notable implications for the properties and performance of the composite material.

3.2. Microstructural Study Using TEM and FTIR

### 3.2.1. TEM Study of the Cs/MMT (1:3) and Cs/HET (1:3) Samples

Transmission electron microscopy (TEM) unveils contrasting interaction dynamics between Cs/MMT (1:3) and Cs/HET (1:3) samples throughout the synthesis process.

Cs/MMT (1:3): After one hour, TEM images of Cs/MMT reveal a uniform structure with well-distributed chitosan (yellow circle) and montmorillonite crystallites (red circle), indicating immediate interaction (Figure 5). This contrasts sharply with Cs/HET, where TEM images show distinct phases with no interaction between hectorite and chitosan after one hour, aligning with the XRD data suggesting minimal exfoliation in Cs/HET (Figure 6).

Over time, Cs/MMT undergoes a continuous transformation. By the two-hour mark, Cs/MMT exhibits clear signs of exfoliation, with layer separation increasing around the organic component. This progressive interaction between chitosan and montmorillonite intensifies at three hours, leading to maximum exfoliation by four to five hours. TEM images effectively capture this transformation, showcasing the formation of a well-established and stable nanocomposite. In contrast, Cs/HET displays a more gradual interaction process. Initially segregated, the TEM images reveal a gradual shift towards interaction between chitosan and hectorite crystallites, starting at the two-hour mark. Similar to Cs/MMT, Cs/HET achieves maximum exfoliation in four to five hours, resulting in a stable nanocomposite. However, the slower kinetic interaction between chitosan and hectorite compared to montmorillonite is evident throughout the process. In conclusion, TEM analysis highlights the significant influence of clay type on the interaction kinetics and overall transformation process. Cs/MMT exhibits a swifter and more uniform interaction with chitosan, while Cs/HET undergoes a slower but progressive interaction, ultimately achieving a stable nanocomposite structure [15,34,61].
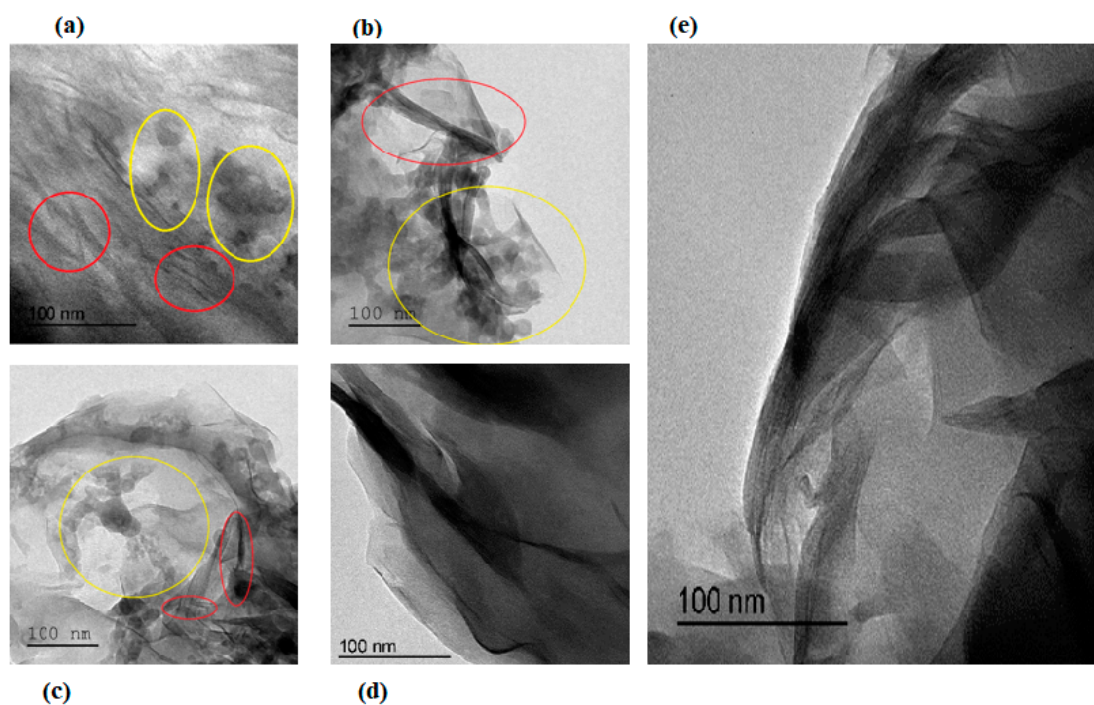
Figure 5. TEM images related to the kinetics of the preparation of the Cs/MMT sample (1:3); (**a**) after 1 h, (**b**) after 2 h, (**c**) after 3 h, (**d**) after 4 h, and (**e**) after 5 h.
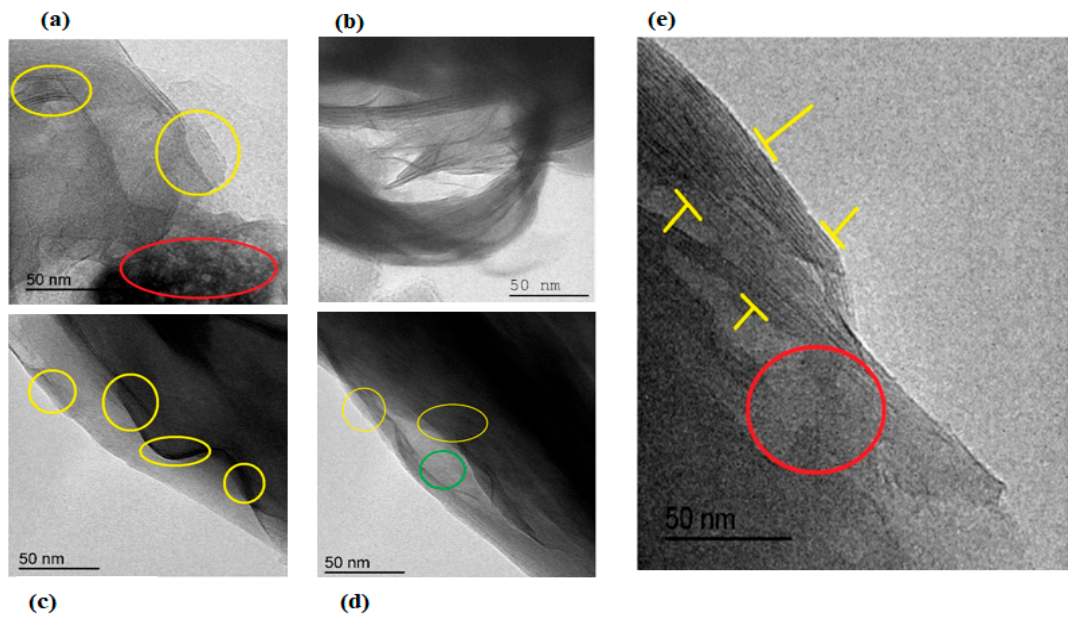
Figure 6. TEM images related to the kinetics of the preparation of the Cs/HET sample (1:3); (**a**) after 1 h, (**b**) after 2 h, (**c**) after 3 h, (**d**) after 4 h, and (**e**) after 5 h.

The comparative analysis of EDX (energy-dispersive X-ray spectroscopy) results (Table 2 and Figure 7) confirms the observations made by electron microscopy. For the CS/MMT sample, during the initial hour of synthesis, the absence of characteristic nitrogen peaks and the low presence of carbon from the polymer are consistent. This observation aligns with the predominance of the mineral fraction in the initial stoichiometry and suggests a slow reaction rate. However, after one hour of reaction, the emergence of a nitrogen peak, albeit of low intensity, likely indicates the exfoliation of clay layers, leading to a reduction in crystallite size and the appearance of a clear nitrogen fraction. This evolution is consistent with TEM observations, which demonstrated progressive exfoliation and increased interaction between chitosan and montmorillonite over time. This interpretation is also supported by the XRD results for the same sample. Additionally, the decrease in the mass fraction of exchangeable sodium and chlorine present in the interlayer space of the clay after pretreatment confirms this.

Table 2. Elemental analysis of the CS/MMT and CS/HET obtained by energy-dispersive spectrometry (EDX) coupled to TEM at 1 h and 5 h.

Element Sample	C	N	O	Na	Mg	Al	Si	Cl	Ca	Fe	Total (wt%)
CS/MMT_1h	5.87	0.10	36.13	5.75	2.43	12.24	31.52	2.74	n.d	3.22	100
CS/MMT_5h	7.12	1.27	36.38	4.89	2.08	11.92	31.04	2.43	n.d	2.87	100
CS/HET_1h	3.81	0.88	41.02	3.61	3.11	10.71	28.49	1.58	3.18	3.61	100
CS/HET_5h	3.92	2.57	39.46	4.36	1.78	11.02	27.01	1.92	4.14	3.82	100

n.d. indicates that the element was not detected or could not be determined within the limitations of the analysis.

For the CS/HET sample under the same synthesis and EDX characterization conditions, the presence of characteristic peaks of the polymer phase is observed, with intensities reflecting the initial 1:3 stoichiometry. This differs from the CS/MMT sample and is likely due to the nature of occupancy in the octahedral cavity of hectorite. The nitrogen peak is observable after one hour of reaction, indicating a faster reaction rate compared to montmorillonite.

Furthermore, the exfoliation of layers is confirmed by the appearance of a nitrogen-associated peak after one hour of synthesis. This observation corresponds with TEM results, which showed a progressive interaction between chitosan and hectorite, ultimately leading to a stable nanocomposite structure. In summary, the comparative analysis between electron microscopy and EDX results highlights the correlation between the evolution of interactions observed at the nanoscale and changes in the chemical composition of the samples, thereby confirming the mechanisms of formation of CS/MMT and CS/HET nanocomposites during the synthesis process.
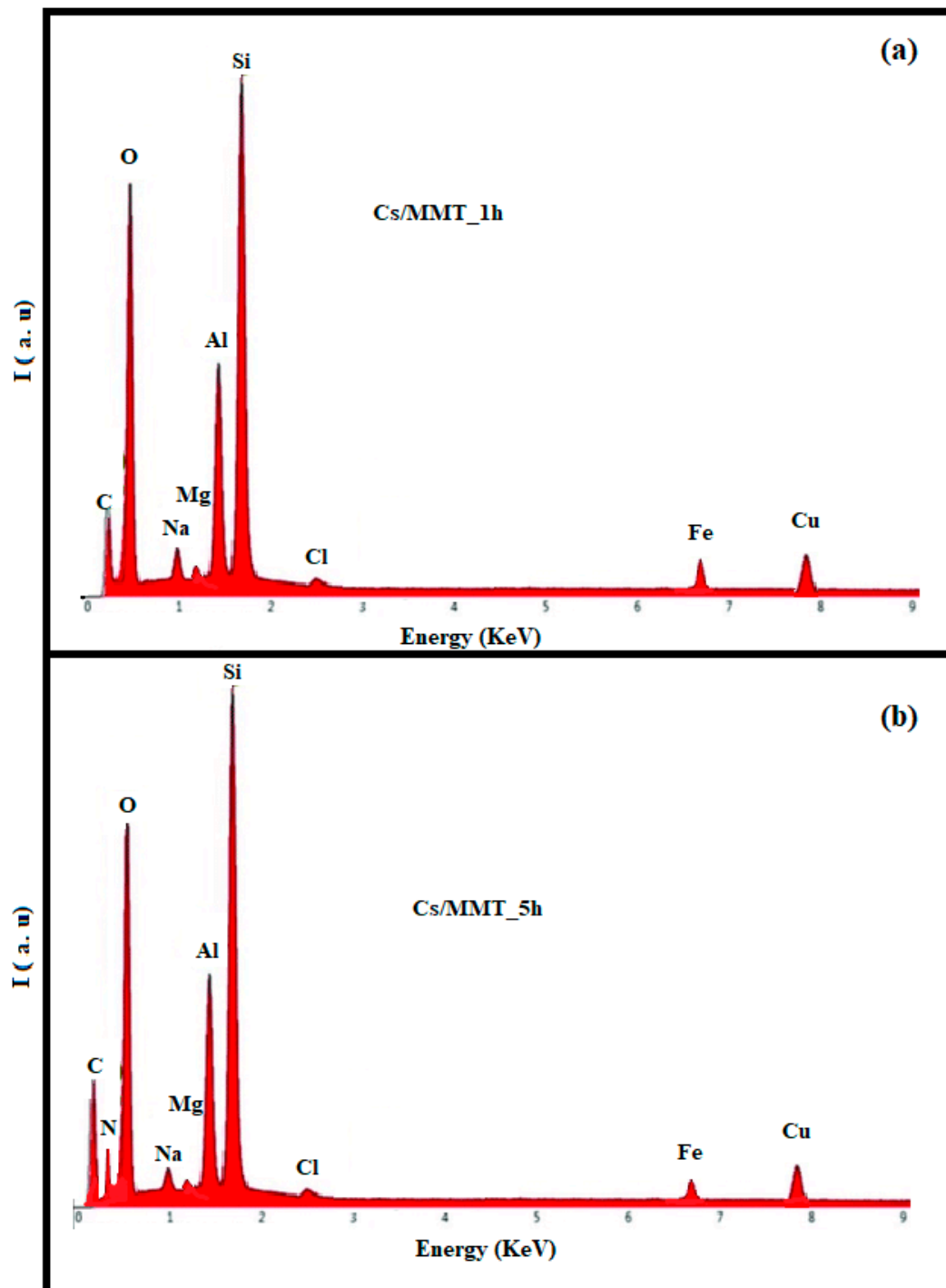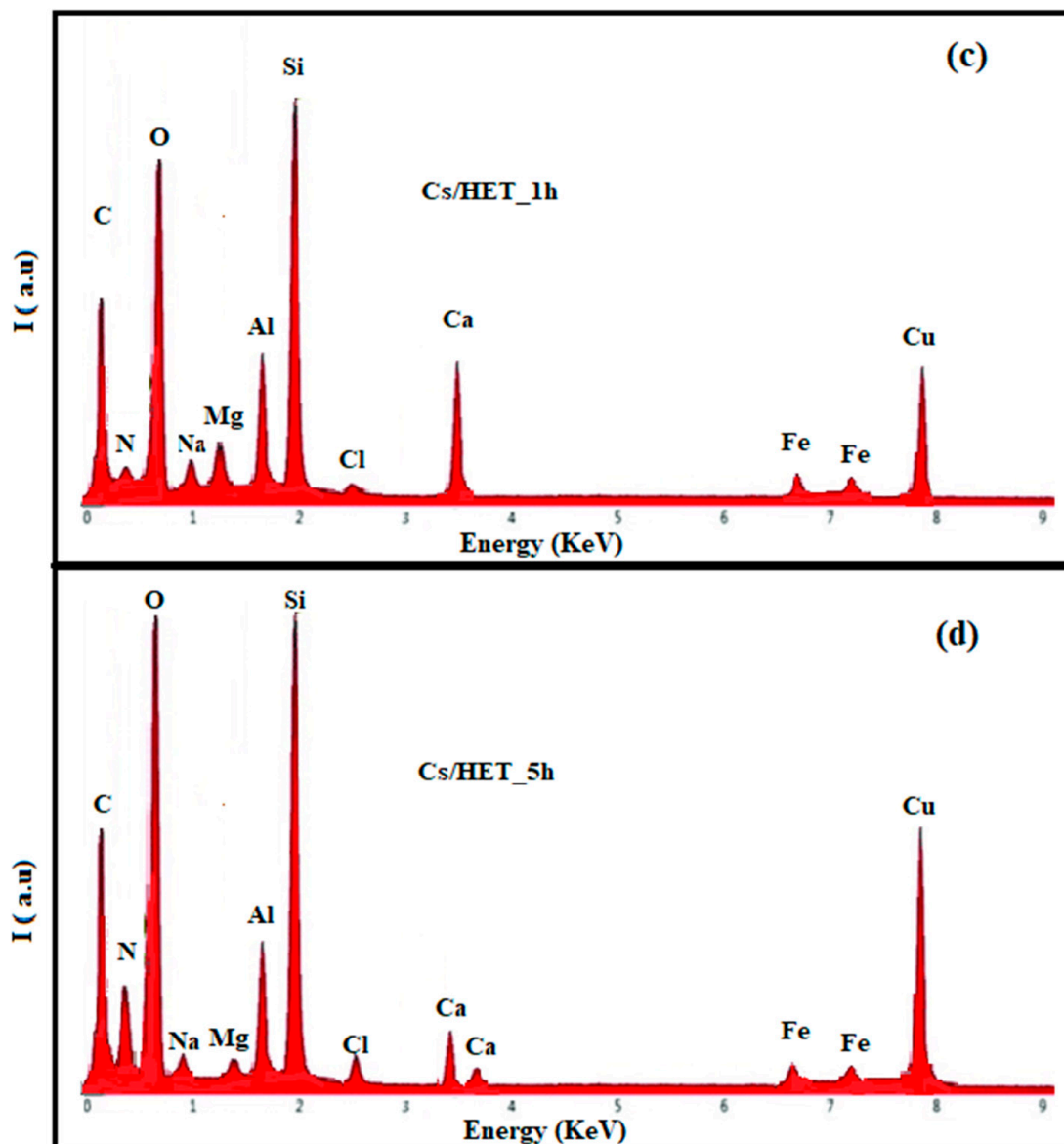

Figure 7. *Cont.*

Figure 7. The EDX spectra of synthesized nanocomposite (**a**) Cs/MMT (1:3) after 1 h reaction time, (**b**) Cs/MMT (1:3) after 5 h reaction time, (**c**) Cs/HET (1:3) after 1 h reaction time, and (**d**) Cs/HET (1:3) after 5 h reaction time.

3.2.2. Characterization through FTIR of the Effect of Kinetics Reaction
Case of the Cs/MMT (1:3) and Cs/HET (1:3) Sample

FTIR analysis of Cs/MMT (1:3) and Cs/HET (1:3) nanocomposites (Figures 8 and 9) reveals both commonalities and contrasting interaction trends. While both exhibit characteristic bands for chitosan and clay components, the Cs/MMT spectra (Figure 7) show increasing band intensity with reaction time, suggesting ongoing interaction and potential new bond formation. Conversely, the Cs/HET spectra (Figure 8) display a decrease in band intensity, particularly for chitosan's amide II bond, implying potential disruption or deformation during synthesis. Additionally, the presence of a Si-O-Al bond (~500 cm^{-1}) solely in Cs/MMT confirms the distinct structure of montmorillonite compared to hectorite. Overall, FTIR analysis highlights the following contrasting interaction dynamics: Cs/MMT demonstrates progressive interaction, while Cs/HET exhibits a weakening interaction with reaction time, influencing the final structure and properties of the synthesized nanocomposites [15,34,63,64].
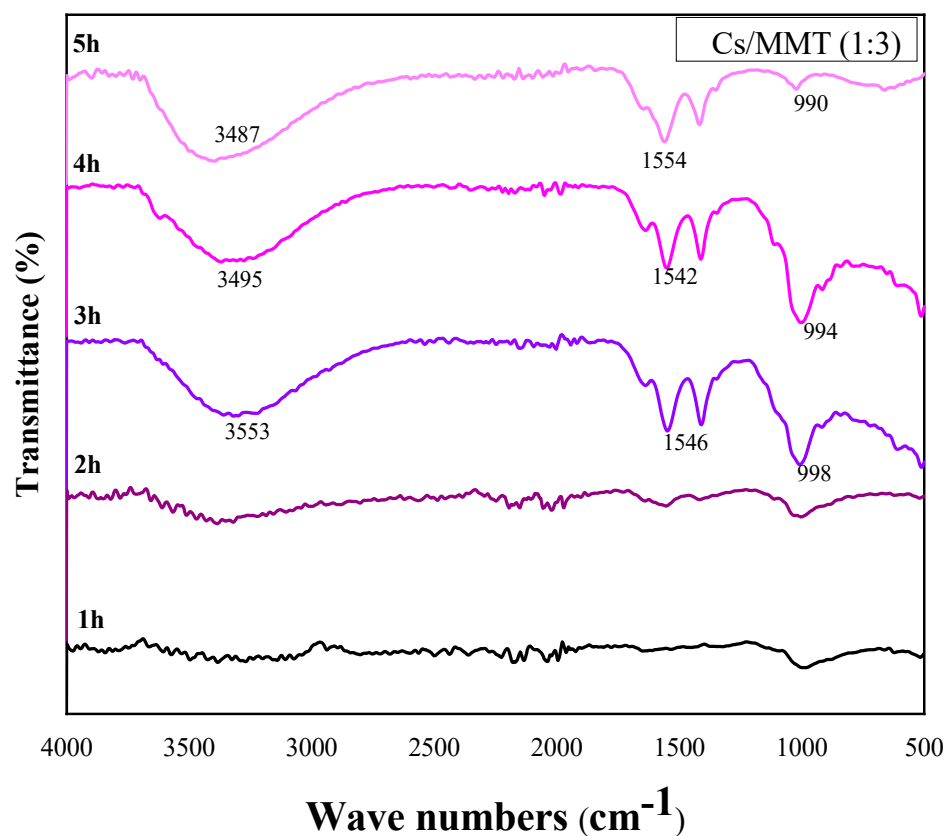
Figure 8. IR transmission spectra of Cs/MMT (1:3)_1h, Cs/MMT (1:3)_2h, Cs/MMT (1:3)_3h, Cs/MMT (1:3)_4h, and Cs/MMT (1:3)_5h.
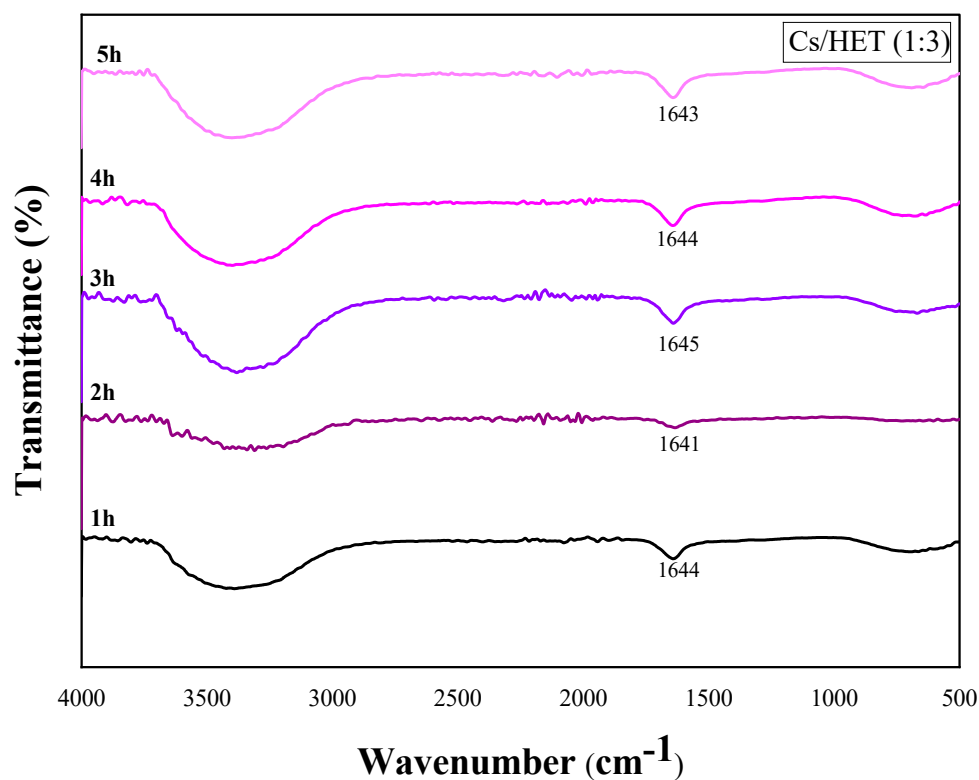
Figure 9. Transmission IR spectra of Cs/HET (1:3)_1h, Cs/HET (1:3)_2h, Cs/HET (1:3)_3h, Cs/HET (1:3)_4h, and Cs/HET (1:3)_5h.

3.3. Photocatalytic Activity

3.3.1. Effect of Reaction Kinetics on Dye Degradation

The kinetic data strikingly unveil the evolving dynamics orchestrated by the degradation of Brilliant Yellow Cibacron 3GP dye under irradiation. By examining samples subjected to various time intervals (1 h, 2 h, 3 h, 4 h, and 5 h), it is evident that their absorbance gradually decreases, a telling sign of the dye's progressive deterioration. This reduction in intensity visually illustrates the ongoing degradation process. Particularly noteworthy is that the intensification of this destructive phenomenon becomes markedly more pronounced as the exposure duration increases, highlighting a direct correlation between the reaction kinetics and the degradation efficiency. This significantly underscores that both the rate and extent of the degradation process are profoundly influenced by two key factors: the exposure duration and the degree of agitation. These interdependent elements are captured and depicted in Figure 10, Figure 11 and Figures S1–S9, offering a visual perspective on how the reaction kinetics shape the evolution of the dye degradation process.

Cs/MMT Sample

In the context of organic contaminants, TiO_2 demonstrated a notable 32% degradation efficiency within the chitosan–montmorillonite nanocomposites (Figure 10a). This observation signifies that TiO_2 possesses the capability to effectively degrade a portion of the organic contaminants present in the samples when employed as a photocatalyst. Depending on the specific application scenario, a 32% degradation rate may hold significant value, highlighting TiO_2's capacity to generate electron–hole pairs that actively contribute to the decomposition of organic molecules. In contrast, ZnO (Figure 10b) exhibited a slightly lower degradation efficiency of 23%. This disparity suggests that, within the given context of chitosan–montmorillonite nanocomposites, ZnO is comparatively less proficient in degrading organic pollutants. Nonetheless, ZnO retains the capacity to catalyze photocatalytic degradation processes, albeit with a reduced degradation rate compared to TiO_2 (Figure 10).
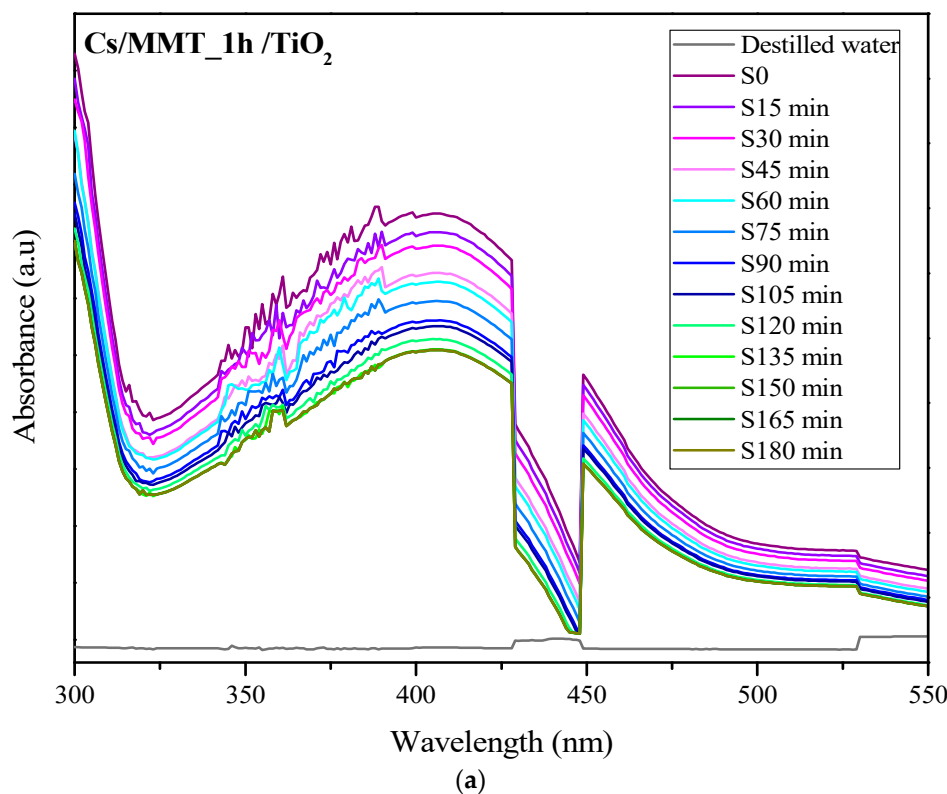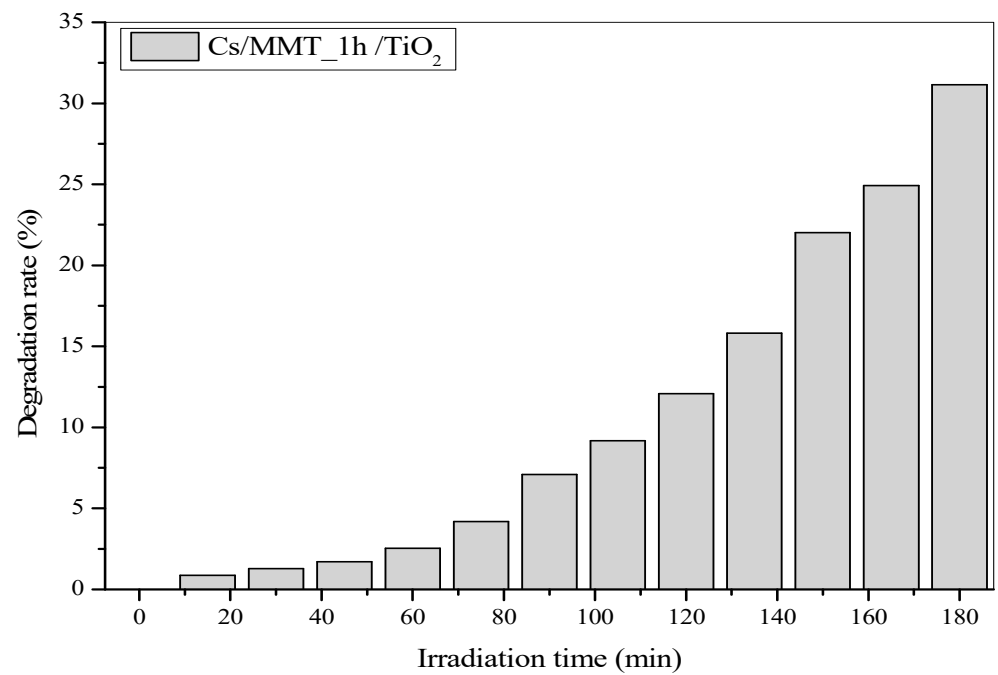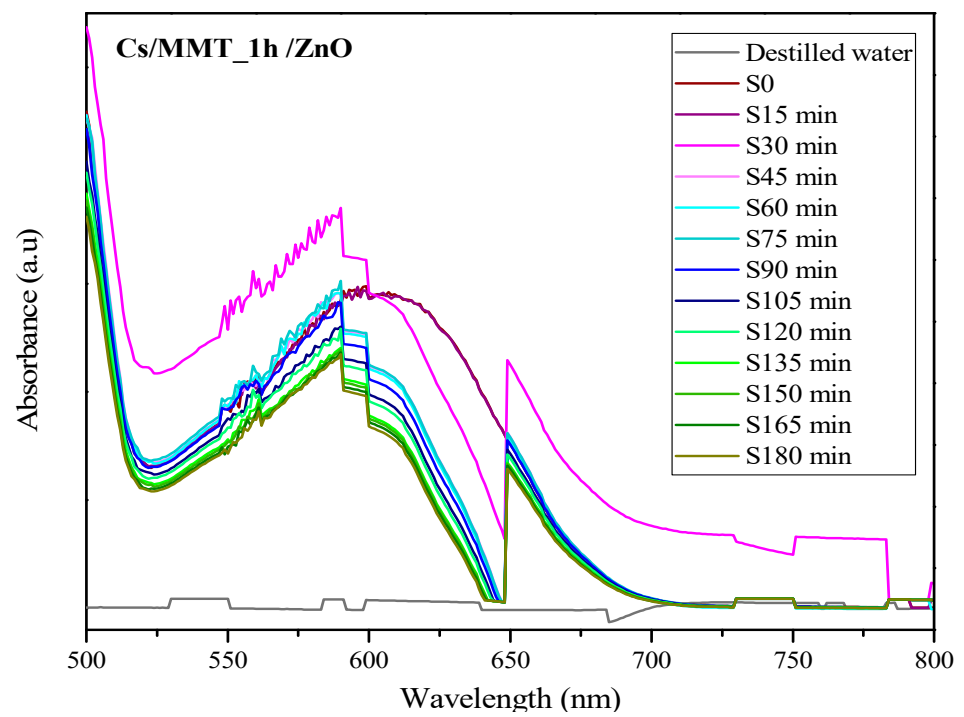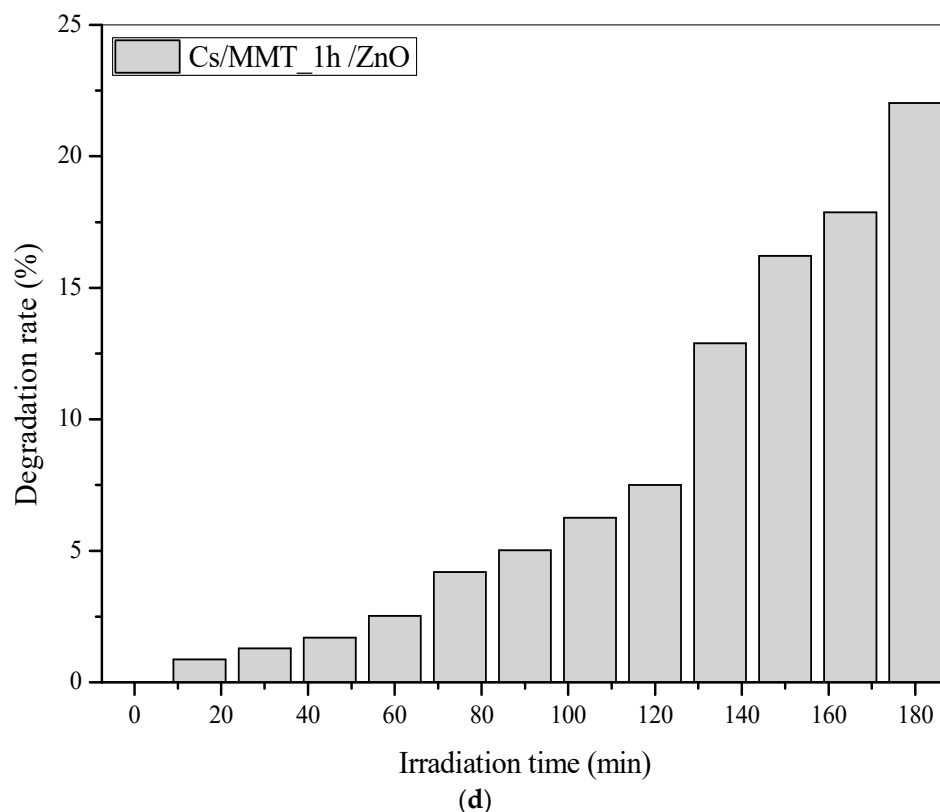

Figure 10. *Cont.*

(**b**)

(**c**)

Figure 10. *Cont.*

Figure 10. (**a**) Catalytic degradation of CBY3G-P by Cs/MMT nanocomposites for 1 h in the presence of TiO$_2$, (**b**) photocatalytic degradation rate of CBY3G-P dye on Cs/MMT, TiO$_2$ for 1 h under 180 min of irradiation, (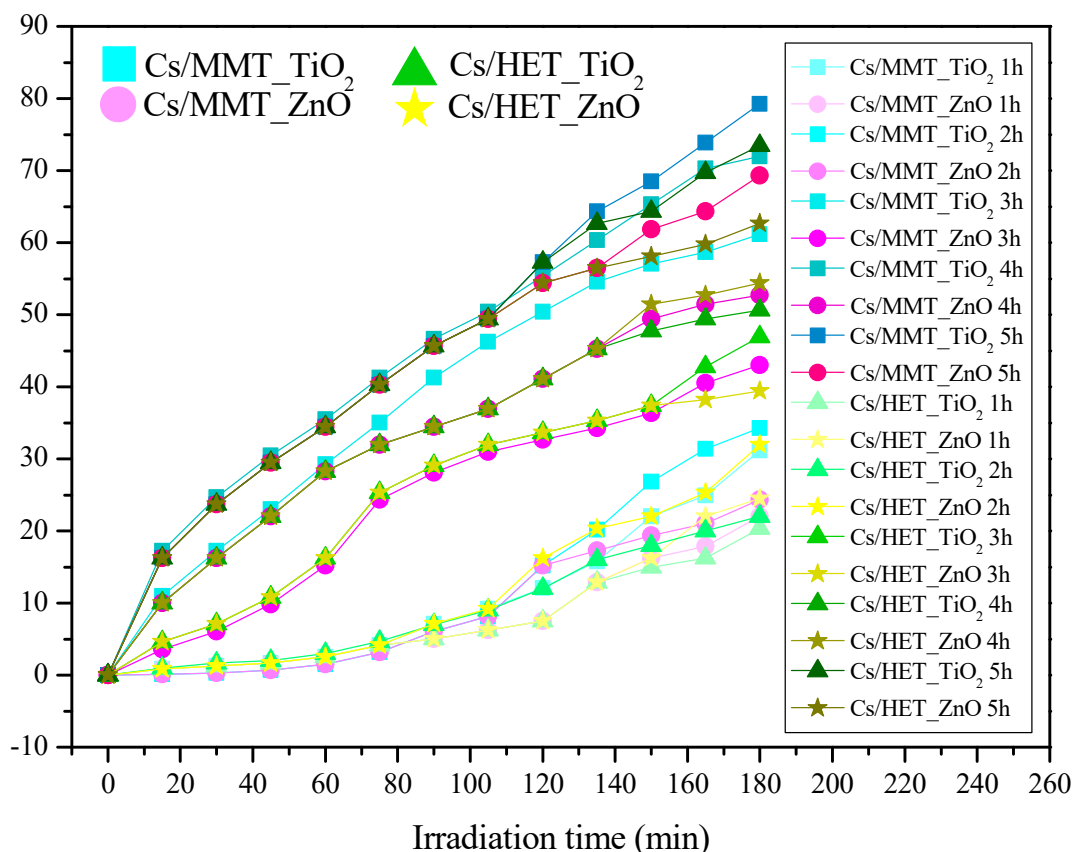**c**) catalytic degradation of CBY3G-P by Cs/MMT nanocomposites for 1 h in the presence of ZnO, and (**d**) photocatalytic degradation rate of CBY3G-P dye on Cs/MMT, ZnO for 1 h under 180 min of irradiation.

By extending the agitation time during the synthesis of chitosan–montmorillonite nanocomposites from 1 to 2 h (Figure S1), there was a marginal uptick in the degradation rate for ZnO, from 23% to 25%, and a more substantial rise for TiO$_2$, from 32% to 37%. Regarding ZnO, the increased agitation time had a modest impact on its efficacy in degrading organic pollutants. Although the difference in degradation rates between 23% and 25% is relatively small, it suggests a positive response of ZnO to prolonged reaction time. This could be attributed to the extended duration allowing for improved interaction between ZnO and organic pollutants, thereby facilitating degradation. In contrast, TiO$_2$ exhibited a more pronounced enhancement in efficiency with the extended agitation time, escalating from 32% to 37%. This more substantial increase indicates that TiO$_2$ is particularly sensitive to prolonged reaction time. It likely had more opportunity to generate electron–hole pairs under UV irradiation, resulting in a more efficient degradation of organic pollutants.

Increasing the agitation time from 2 h to 3 h (Figure S2) exerted a remarkable impact on the photocatalytic degradation rate of chitosan–montmorillonite nanocomposites, yielding impressive results. The degradation rate surged from 23% to 45% for ZnO and from 37% to an impressive 60% for TiO$_2$ (Figure 10). For ZnO, the extension in agitation time from 2 h to 3 h resulted in a noteworthy enhancement in its efficacy in degrading organic pollutants. The degradation rate leaped from 23% to 45%, signifying a substantial 22% increase. This enhancement can be attributed to the additional time that allowed ZnO to engage with organic pollutants over an extended period, leading to a more potent degradation process. This positive response to prolonged reaction times underscores ZnO's suitability for applications necessitating extended reaction durations. In comparison, TiO$_2$ exhibited an even more significant surge in efficiency with the extended agitation time, elevating from 37% to an impressive 60%, marking a notable 23% increase. This substantial

improvement underscores the particular sensitivity of TiO$_2$ to extended reaction durations. The supplementary time afforded TiO$_2$ the opportunity to generate a greater number of electron–hole pairs, consequently enhancing the efficiency of organic pollutant degradation. TiO$_2$ emerged as an exceptional choice for applications demanding swift and effective degradation, especially in situations where extended reaction times are feasible.

Figure 11. Photocatalytic degradation rate of CBY3G-P dye in the case of Cs/MMT and Cs/HET (catalysts TiO$_2$ and ZnO) versus irradiation time.

When the agitation time was extended to 4 h (Figure S3), a notable upswing in the photocatalytic degradation rate was observed for both semiconductors, ZnO and TiO$_2$, reaching approximately 52% for ZnO and 73% for TiO$_2$. For ZnO, prolonging the agitation time to 4 h brought about a substantial enhancement in its efficiency in degrading organic pollutants, achieving a degradation rate of 52%. This improvement stands out significantly when compared to the earlier rates. This marked increase underscores ZnO responsiveness to extended reaction durations. With more time for interaction with organic pollutants, ZnO demonstrated more effective degradation. ZnO proves to be a fitting choice for applications necessitating prolonged reaction times, such as continuous water or air treatment. Similarly, TiO$_2$ exhibited a noteworthy surge in efficiency with the extended agitation time, attaining an impressive degradation rate of 73%. Once again, this significant enhancement underscores TiO$_2$'s particular sensitivity to extended reaction durations. The supplementary time enabled TiO$_2$ to generate a larger number of electron–hole pairs, thus facilitating highly efficient degradation of organic pollutants. TiO$_2$ emerges as an excellent option for applications where swift and efficient degradation of organic pollutants is imperative, especially when extended reaction times are viable. Further extension of the agitation time to 5 h resulted in a substantial improvement in the photocatalytic degradation rate for both semiconductors, ZnO and TiO$_2$, achieving a degradation rate of 69% for ZnO and 78% for TiO$_2$.

Extending the agitation time to 5 h (Figure S4) resulted in a remarkable enhancement in the efficiency of ZnO in degrading organic pollutants, achieving a degradation rate of 69%. This improvement is notably significant compared to the earlier rates. The substantial surge in the degradation rate highlights ZnO's remarkable sensitivity to extended reaction durations. With ample time for thorough interaction with organic pollutants, ZnO facilitated highly efficient degradation. It establishes ZnO as a highly promising option for applications necessitating in-depth and continuous degradation of organic pollutants, indicating its high material efficiency. Similarly, TiO_2 exhibited a significant boost in its efficiency with the extended agitation time, achieving an impressive degradation rate of 78%. This substantial enhancement once again underscores TiO_2's extreme sensitivity to extended reaction durations. The additional time provided TiO_2 with the opportunity to generate a large number of electron–hole pairs, leading to highly efficient degradation of organic pollutants. TiO_2 emerges as an exceptional choice for applications where rapid and comprehensive degradation of organic pollutants is essential, especially in situations where extended reaction times are feasible.

Cs/HET Sample

In the initial one-hour synthesis of the chitosan–hectorite nanocomposite (Figure S5), both ZnO and TiO_2 semiconductors exhibited low photocatalytic degradation, with a rate of 20% for ZnO and 25% for TiO_2. These initial degradation rates indicate a relatively modest level of organic pollutant degradation in the medium during the first hour of agitation. This suggests that the initial hour of reaction was insufficient to achieve significant pollutant degradation. It is important to note that the low initial degradation rates do not necessarily imply the ineffectiveness of the photocatalytic degradation process. Optimization of results can potentially be achieved by extending the agitation time.

Increasing the agitation time in the synthesis of chitosan–hectorite nanocomposites from 1 h to 2 h (Figure S6) resulted in a notable enhancement in the photocatalytic degradation rate for both semiconductors, ZnO and TiO_2. Specifically, the degradation rate increased from 20% to 22% for ZnO and from 25% to 32% for TiO_2. These results can be interpreted as follows:

The extension of agitation time from 1 h to 2 h led to a subtle yet discernible increase in the degradation rate for ZnO, progressing from 20% to 22%. While this augmentation is relatively modest, it signifies that ZnO exhibits a favorable response to a slightly prolonged reaction duration. This increment may be attributed to the additional time facilitating improved interaction between ZnO and the organic pollutants, resulting in a marginal enhancement in degradation efficiency. It can be inferred that ZnO may find suitability in applications where a moderately extended reaction time is viable, though it is plausible that it approaches its peak efficiency at this juncture.

In contrast, TiO_2 displayed a more pronounced surge in efficiency with the escalation of agitation time, escalating from 25% to 32%. This advancement is notably more substantial than what was observed for ZnO. The considerable improvement strongly suggests that TiO_2 is particularly responsive to an extended reaction time. The supplementary time afforded TiO_2 the opportunity to generate a greater number of electron–hole pairs under UV irradiation, consequently promoting a more efficient degradation of organic pollutants. This highlights TiO_2 as an excellent choice for applications necessitating rapid and thorough degradation, especially under conditions of extended reaction times.

The variation in agitation time from 2 h to 3 h during the synthesis process of chitosan–hectorite nanocomposites (Figure S7) resulted in a noteworthy upswing in the photocatalytic degradation rate for both semiconductors, ZnO and TiO_2. Specifically, the degradation rate increased from 22% to 40% for ZnO and from 32% to 46% for TiO_2. The extension of agitation time from 2 h to 3 h led to a substantial surge in the degradation rate for ZnO, from 22% to 40%. This augmentation underscores the high sensitivity of ZnO to an extended reaction period. The heightened degradation rate can be attributed to the additional time allowing for more extensive and effective interaction between ZnO and

organic pollutants, culminating in a more thorough degradation. These results signify that ZnO proves to be an effective choice for applications requiring a 3 h reaction time, demonstrating a notable efficiency improvement at this stage. Likewise, TiO_2 exhibited a substantial increase in efficiency with the prolongation of agitation time, surging from 32% to 46%. This escalation reaffirms that TiO_2 is highly responsive to an extended reaction time. Upon further extending the agitation time to 4 h in the synthesis of chitosan–hectorite nanocomposites, a significant elevation in the photocatalytic degradation rate was observed for both semiconductors, ZnO and TiO_2. Specifically, the degradation rate increased from 40% to 50% for ZnO and from 46% to 54% for TiO_2 (Figure 10).

The extension of agitation time from 3 to 4 h notably boosted the degradation rate for ZnO, from 40% to 50% (Figure S8). This enhancement is substantial, highlighting ZnO's positive response to prolonged reaction periods. The considerable surge in degradation rate implies that the extra time facilitated extended and more effective interaction between ZnO and organic pollutants, leading to more comprehensive degradation. These findings strongly advocate ZnO as an exceptionally efficient option for applications necessitating a 4 h reaction time, demonstrating remarkable proficiency at this stage. In parallel, TiO_2 exhibited a noteworthy uptick in efficiency with the lengthening of agitation time, advancing from 46% to 54%. This increase underscores TiO_2's high sensitivity to extended reaction periods.

With the extension of agitation time to 5 h in the synthesis of chitosan–hectorite nanocomposites (Figure S9), both semiconductors, ZnO and TiO_2, achieved their peak rates of photocatalytic degradation. At this juncture, ZnO attained a degradation rate of approximately 62%, while TiO_2 reached a remarkable rate of 73%. Extending the agitation time to 5 h proved highly advantageous for ZnO, resulting in its highest degradation rate of 62%. This outcome underscores ZnO's extreme sensitivity to prolonged reaction periods. The noteworthy degradation rate of ZnO at 5 h suggests that the additional time facilitated extensive and effective interaction between ZnO and organic pollutants, leading to thorough degradation. ZnO emerges as an exceptionally efficient option for applications where a 5 h reaction time is viable, demonstrating outstanding proficiency at this stage. Similarly, TiO_2 exhibited a substantial increase in efficiency with prolonged agitation time, culminating in its highest degradation rate of 73% at 5 h. This high degradation rate of TiO_2 at 5 h indicates that the extra time permitted the generation of a substantial number of electron–hole pairs, promoting exceedingly effective degradation of organic pollutants. TiO_2 distinguishes itself as an exceptional choice for applications necessitating rapid and thorough degradation of organic pollutants, particularly when extended reaction times are feasible.

The photocatalytic performance of a TiO_2-based nanocomposite depends on several factors, such as particle size, material interface, crystalline structure, presence of co-catalysts, stability, and synthesis conditions. The lamellar structure of montmorillonite (MMT) and its higher TiO_2 content compared to hectorite (HET) make it more susceptible to degradation. This increased degradation can affect its photocatalytic performance in the long term. In summary, the photocatalytic properties of a nanocomposite depend not only on the presence of TiO_2 but also on a synergy of intrinsic and extrinsic factors. The material's structure, chemical composition, synthesis conditions, the presence of co-catalysts, and material stability play a crucial role (Table 3).

Table 3. Comparison between samples.

| Samples	Experimental Conditions	Decolorization (%)	Refs.
TiO_2/MMT	Light = 250 W mercury lamp; MMT = 40 mg L^{-1}; V = 0.5 L; t = 135 min	100.00	[65]
TiO_2/MMT	Light = 30 W mercury lamp; MMT = 20 mg L^{-1}; V = 0.01 L; t = 50 min	100.00	[66]
TiO_2/Cs	Light = 6 W mercury lamp; MMT = 10 mg L^{-1}; V = 0.15 L; t = 75 min	70.00	[67]
TiO_2/Cs	Light = solar simulator; MMT = 16.4 mg L^{-1}; V = 1 L; t = 120 min	063.60	[68]
Cs/MMT (1:3)_1h	Light = 230 W mercury lamp; MMT = 75 mg L^{-1}; V = 0.05 L; t = 180 min	024.12	
Cs/MMT (1:3)_5h	Light = 230 W mercury lamp; MMT = 75 mg L^{-1}; V = 0.05 L; t = 180 min	069.27	Our work
Cs/HET (1:3)_1h	Light = 230 W mercury lamp; MMT = 75 mg L^{-1}; V = 0.05 L; t = 180 min	024.16	
Cs/HET (1:3)_5h	Light = 230 W mercury lamp; MMT = 75 mg L^{-1}; V = 0.05 L; t = 180 min	062.51	

3.3.2. Photocatalytic Efficiency and Catalyst Type

The apparent differences in performance between the two semiconductor photocatalysts, specifically TiO_2 and ZnO, are depicted graphically in Figure 11. Particularly, samples with TiO_2 treatment degrade Cibacron Brilliant Yellow 3GP dye much more quickly than samples with ZnO. This discrepancy provides unmistakable proof of TiO_2 supremacy in terms of photocatalytic activity within the particular parameters of this reaction. Furthermore, Figure 11 highlights the differences between the two types of nanocomposites, Cs/MMT and Cs/HET, in terms of how well they degraded the Cibacron Brilliant Yellow 3GP dye. In contrast to ZnO, TiO_2 consistently outperforms ZnO in both versions of nanocomposites, suggesting that the choice of support has less of an effect on TiO_2 performance. This finding shows that, unlike ZnO, which exhibits more variable efficiency depending on the supporting material, the degradation process accelerated by TiO_2 appears to be less dependent on the type of support used. In conclusion, our thorough research convincingly demonstrates the significant impact of the catalyst's inherent properties on photocatalytic efficiency while also illuminating the differences in interactions between the catalytic materials and their distinct support matrices.

3.3.3. Relationship between Photocatalytic Performance and Octahedral Cavity Occupation of the Starting Clay Fraction

Figure 12 encapsulates the overarching trends discerned from our results. A prominent conclusion is evident: TiO_2 emerges as the catalyst of choice for the degradation process, particularly when coupled with the dioctahedral charge nanocomposites Cs/MMT. This graphical representation consolidates and provides a coherent overview of the patterns observed throughout this study. Upon meticulous examination, Figure 12 enables the deciphering and emphasis of significant relationships and comparisons across various experimental conditions.

One salient deduction is the exceptional performance of TiO_2 as the favored catalyst for the degradation of the dye Cibacron Brilliant Yellow 3GP. This conclusion stems from the markedly higher degradation rates achieved with TiO_2 in contrast to ZnO across diverse experimental setups. This divergence in photocatalytic efficacy can be attributed to a fundamental dissimilarity in the crystalline structures of the employed clays. Montmorillonite, a dioctahedral charge clay, contrasts with hectorite, which exhibits a trioctahedral nature. This incongruity in the occupancy rate of the octahedral cavity by ions directly impacts behavior and photocatalytic efficiency. The observed discrepancies in performance can be explained by the major influence that this unique structural attribute has on the interactions between catalytic materials and their respective supports. In summary, Figure 12 visually

elucidates this intricate dynamic, pinpointing TiO_2 as the preferred catalyst owing to its superior efficiency while underscoring the pivotal role played by the nature of the support in the performance of photocatalytic catalysts.
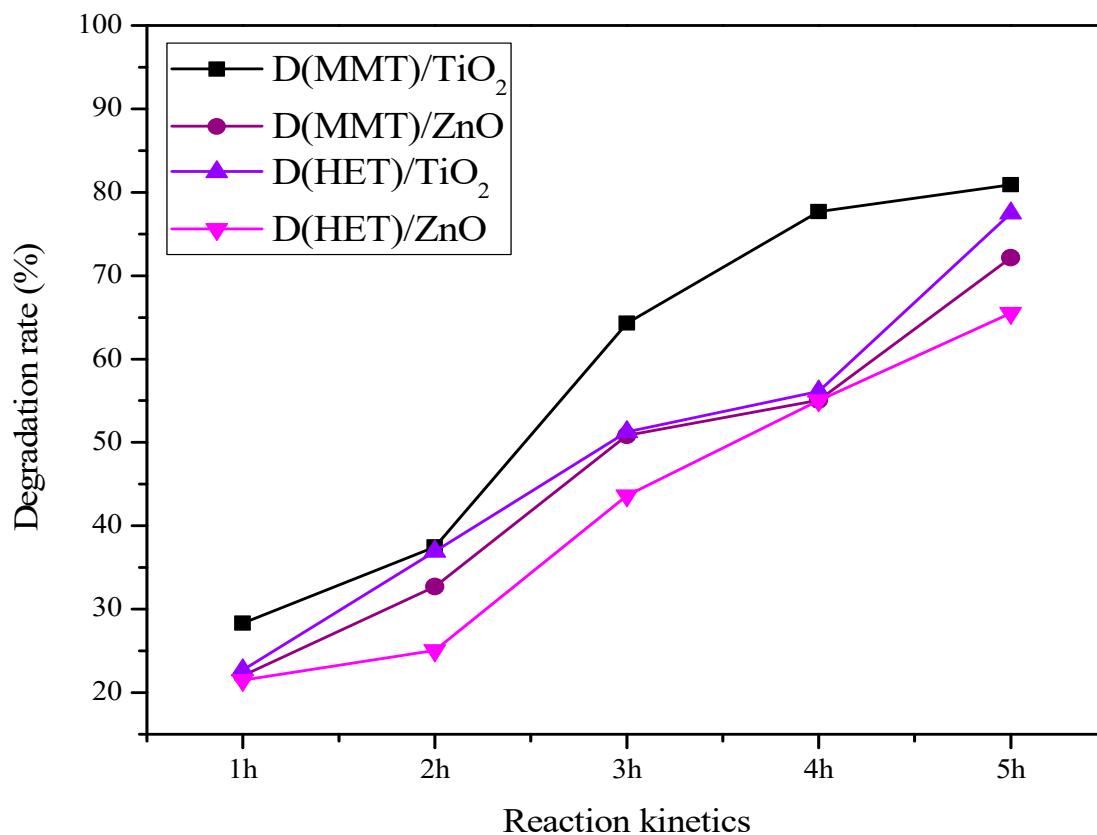
Figure 12. Correlation of results comparing the photocatalytic activity of different samples after 180 min of irradiation.

In this study, the stability of the samples is a crucial element, and to validate it, we have implemented a series of measures at various stages of the reaction. First, each manipulation was carried out with methodological rigor to ensure the reproducibility of the results. Furthermore, all manipulations were conducted under consistent atmospheric conditions for all samples, including humidity, temperature, and pressure, to minimize external variations that could influence the results. Additionally, a systematic blank test was performed before each radiographic recording, involving two passes of each sample under the diffractometer, spaced one hour apart. If any structural anomaly or difference in diffraction profiles was observed, it called into question the integrity of the entire manipulation, typically resulting in the experimental procedure being restarted from the beginning, regardless of the reaction kinetics (Figure 1).

4. Discussion

4.1. Utilizing Reaction Kinetics Assessment Tools to Optimize Nanocomposite Efficiency

Over the past 10 years, there has been a great deal of success with the use of chitosan/clay nanocomposites in environmental applications. The focus of research has been on agri-food and antibacterial uses [69]. However, the ability to integrate structural and physicochemical features from both organic and inorganic materials with nanoclays opens the door to improving numerous functionalities (such as mechanical, barrier, and antioxidant capabilities) of chitosan-based films and coatings. To achieve good adsorptive or degradative activity in the presence of organic molecules, the production of these nanocomposites has been optimized [34]. The success of the synthesized product is directly related to

the decision to use the synthesis process and the method by which the application is carried out. The most commonly employed method for producing chitosan–clay nanocomposite films is solution casting, which is both cost-effective and straightforward to prepare. The approach utilized in this article aligns with this technique, underscoring its efficiency and applicability in nanocomposite film production [34,70,71]. A versatile method for creating thin coatings with mixed functional properties of various polymers is layer-by-layer (LbL) self-assembly [72]. Hydrophobic interaction, hydrogen bonding, van der Waals forces, and electrostatic interactions are among the mechanisms of deposition that depend on mutual attraction between layers [73]. The cationic and hydrophilic properties of chitosan in acidic environments enable high miscibility with negatively charged nanoclays, including Montmorillonite (MMT) platelets, in chitosan–clay nanocomposites [74]. Solutions can be sprayed over the substrate or submerged to accomplish experimental deposition [75]. Although studies employing LbL deposition for chitosan–clay nanocomposite films are limited, the approach exhibits potential for film creation [74]. The mechanical, barrier, antioxidant, and antibacterial properties of chitosan-based films can all be enhanced by incorporating nanoclays at an optimized initial stoichiometry. This is demonstrated in this study by establishing an optimized starting stoichiometry and delving further into quantifying the kinetics of the reaction, enabling the tracking of structural evolution and precise identification of the link between structure and photocatalytic effectiveness. The three fundamental structures—tactoid, intercalation, and exfoliation—have a strong correlation with the physicochemical characteristics of chitosan–clay nanocomposites, which is pertinent to note [76–78]. In accordance with the cited references, the same group of authors has previously worked on the optimization of the initial stoichiometry (from a structural standpoint) [34]. A highly detailed process that allowed reactant concentrations to be adjusted in accordance with possible applications made this synthesis possible [34]. The results of these experiments form the basis of this research, which attempts to improve the control and optimize the synthesis. Specifically, a starting stoichiometry of 1:3 was employed. After the synthesis reaction time was optimized by spaced-time samplings, we were able to fully comprehend the changes that affected the structure and even the photocatalytic performance in the presence of Cibacron Brilliant Yellow 3GP dye. Indeed, characteristic features of a nanocomposite emerge as early as the first hour of synthesis, demonstrating photocatalytic activity in the presence of ZnO or TiO_2. The nanocomposite efficiency increases regardless of the semiconductor used as a function of reaction time. This adaptation has made it possible to objectively define the synthesis time, which was, to the best of our knowledge, frequently addressed in qualitative terms in all earlier research.

4.2. Synchronized Influence of Clay Nature, Octahedral Cavity Occupancy, Initial Stoichiometry, Metal Oxide Type, and Polymer Concentration on Photocatalytic Efficiency in Nanocomposites

Previous studies have made significant contributions to understanding the photocatalytic activity of clay and clay–polymer nanocomposites combined with metal oxide nanoparticles. For instance, [79] highlighted the formation of a robust photocatalyst resulting from the heterojunction between ZnO/TiO_2 semiconductor nanoparticles and delaminated layers of natural clay. The obtained results indicate that the nanocomposite exhibits intense adsorption and a notable degradation rate, allowing for the complete decolorization of Methylene Blue in just 10 min. The acquired results corroborate those found during this study. Indeed, apart from the clay and metallic oxide (ZnO or TiO_2), a fraction of the polymer, with an optimally calibrated initial concentration, was employed to underscore the degradative potential of the nanocomposite in the presence of Cibacron Brilliant Yellow 3GP dye.

Similarly, the study by [80] emphasizes the significance of clay-based nanocomposites incorporating TiO_2 and ZnO in pioneering water treatment processes, highlighting the potential of nanostructured filters for water treatment applications. In this context, our contribution is characterized by the optimization of the initial stoichiometry between chitosan and clay (1:3) and an in-depth investigation into the effect and efficacy of the

starting clay's nature, particularly concerning the occupancy of the octahedral cavity in two distinct smectites. This expansion of knowledge broadens the scope of potential applications in the field.

The study conducted by [81] on the adsorption and photocatalysis of Methylene Blue using a sodium carbonate-activated bentonite adsorbent and a ZnO/bentonite photocatalyst demonstrates an impressive 99.54% degradation efficiency with a photocatalyst of an average size of 30.06 nm. However, it is important to note that this study overlooks the potential influence of the polymer fraction in the nanocomposite synthesis process. This leads to results that are highly specific and limited to localized effects. While clay proves to be an effective porous medium for adsorption and degradation, the properties of the nanocomposite remain somewhat restricted due to the oversight of the enhanced mechanical characteristics provided by the presence of the polymer fraction. In contrast, our study, building upon the foundation laid by the same authors in their previous studies [34], introduces a novel aspect. We achieve highly encouraging degradation rates through the optimization of a complex structure, offering a more comprehensive understanding of the nanocomposite's capabilities.

In recent investigations, ref. [82] explored the suppression of photocatalytic activity by encapsulating TiO_2 nanoparticles with chitosan using a spray-drying method, targeting potential applications in sunblocking. The study revealed a significant reduction in photoactivity for chitosan-encapsulated nanoparticles compared to pristine TiO_2, with degradation rates dropping from 95% to 39.5% after 120 min. This highlights the potential of the straightforward coating process and chitosan material as an inactive protective layer for sunblocking applications. Additionally, ref. [83] delved into the adsorption and photocatalytic-conjugated activity of a chitosan-functionalized titanate coating for clonazepam removal from drinking water. Their research evaluated H_2TiO_7 nanotubes functionalized with varying percentages of chitosan, demonstrating a substantial 80.79% removal of clonazepam after 240 min, surpassing both TiNT and commercial TiO_2 powders by 4.38% and 49.64%, respectively. Moreover, the 2TiCN coating exhibited a remarkable 6.88% increase in efficiency after four reuses. The Ref. [84] study focused on the synthesis of chitosan/SnO_2 nanocomposites through chemical precipitation for enhanced visible light photocatalytic degradation of Congo red and rhodamine B dye molecules. Their findings showcased exceptional degradation rates, with 95% degradation of rhodamine B dye within 60 min, significantly outperforming SnO_2 nanoparticles. Furthermore, the chitosan/SnO_2 nanocomposites achieved a remarkable 98% degradation of Congo red dye within 40 min of visible light exposure, underscoring their superior photodegradation capabilities. Ref. [8] provided a comprehensive examination of the physicochemical and photocatalytic properties of the ZnO-bentonite/chitosan hybrid-biocomposite for water remediation under visible light conditions. Their research demonstrated a substantial increase in methyl orange (MO) removal (86.1%) in the presence of a ZnO-bentonite/chitosan hybrid biocomposite, surpassing bentonite (75.8%) and chitosan (65.4%). Under visible light irradiation, the MO removal rate was an impressive 268 times higher compared to ZnO nanoparticles, showcasing the hybrid biocomposite's potential for highly effective water remediation applications. These recent studies have primarily focused on the development of nanocomposites using chitosan and metallic oxides, often overlooking the contribution of the clay fraction. The results obtained, however, unequivocally demonstrate the potential for dye degradation in the presence of these materials, offering valuable insights. They serve as pivotal starting points for our study, which seeks to further investigate the degradation phenomenon of a broader spectrum of organic molecules, incorporating various combinations of polymer, clay, and metallic oxide components to enhance the understanding of organic dye degradation processes.

Incorporating these prior studies within the context of our research underscores the exceptional nature of our contribution. Our investigation has not only optimized the initial stoichiometry between chitosan and clay but has also provided a comprehensive understanding of how the nature of clay profoundly influences the photocatalytic performance.

Notably, our exploration of hectorite-based nanocomposites with such precision in initial concentration is unprecedented in the field. Additionally, we have ventured into uncharted territory by exploiting the effect of octahedral cavity occupancy on the photocatalytic properties of the developed material. Furthermore, our study stands out for its rigorous optimization of the synthesis protocol and nanocomposite architecture, which have been validated across various types of starting clays. This versatility adds a significant dimension to our study, enhancing its applicability and impact. Additionally, we conducted a meticulous comparative analysis of the efficacy of degrading the Cibacron Brilliant Yellow 3GP dye using both ZnO and TiO_2. This comparative approach provides a nuanced understanding of the distinct contributions of these metal oxides to the degradation process. Moreover, the meticulous monitoring of the reaction kinetics has allowed us to fine-tune the synthesis time while maintaining a fixed initial stoichiometry for all components. This optimization process has led to the development of a nanocomposite with superior catalytic potential, setting a new standard in the field. Altogether, our research represents a significant advancement, pushing the boundaries of knowledge in the realm of clay-based nanocomposites and their applications in photocatalysis.

5. Conclusions

This research explores the impact of synthesis kinetics on the structural and photocatalytic properties of chitosan–clay nanocomposites (Cs/MMT) and chitosan–hectorite nanocomposites (Cs/HET), employing an optimized initial stoichiometry of 1:3. A range of analytical techniques, including X-ray diffraction (XRD), transmission electron microscopy (TEM), and Fourier-transform infrared spectroscopy (FTIR), were utilized. Additionally, the photocatalytic performance of the nanocomposites was assessed using semiconductor catalysts TiO_2 and ZnO, focusing on reaction kinetics, catalyst characteristics, and octahedral cavity occupancy of the clay affecting photocatalytic efficiency. The results highlight the significant influence of reaction kinetics on the structural features of the nanocomposites. Notably, the structural evolution of Cs/MMT and Cs/HET was notably affected by reaction duration, with Cs/MMT exhibiting higher crystalline stability compared to Cs/HET due to differences in octahedral cavity occupancy in the initial clays. FTIR and TEM analyses facilitated the observation of component interactions, revealing the progressive evolution of the nanocomposites during the reaction. These findings elucidate how reaction kinetics drive the formation of specific bonds within the nanocomposites.

Regarding photocatalytic activity, this comprehensive study provides insights into the complex dynamics of photocatalytic degradation, with a specific focus on the performance of TiO_2 and ZnO under varied experimental conditions. The results unequivocally demonstrate the superior performance of TiO_2 as a catalyst, particularly when integrated with the dioctahedral charge nanocomposites Cs/MMT. This preference arises from TiO_2 consistently exhibiting higher degradation rates compared to ZnO across various experimental setups. A crucial factor influencing this difference in photocatalytic efficacy lies in the distinct crystalline structures of the utilized clays. The contrasting nature of montmorillonite, a dioctahedral charge clay, with hectorite, exhibiting a trioctahedral nature, significantly impacts the occupancy rate of the octahedral cavity by ions. This structural disparity plays a pivotal role in dictating the interactions between catalytic materials and their respective supports, thereby accounting for the observed variations in performance. The findings underscore the critical importance of selecting an appropriate catalyst and support matrix for photocatalytic processes, with TiO_2 emerging as the preferred catalyst due to its exceptional efficiency. This research emphasizes the need for tailored catalyst-material combinations to optimize performance in specific applications. Overall, this study offers valuable insights into the intricate interplay of catalyst properties and support matrices in photocatalytic processes, paving the way for more efficient and targeted applications in environmental remediation and other fields requiring effective pollutant degradation.

Supplementary Materials: The following supporting information can be downloaded at: https://www.mdpi.com/article/10.3390/solids5020015/s1, Table S1: The commercialized CS specifications given by the supplier (Glentham life sciences (Wiltshire, UK)); Figure S1: (a) Catalytic degradation of CBY3G-P by Cs/MMT nanocomposites for 2 h in the presence of TiO_2, (b) Photocatalytic degradation rate of CBY3G-P dye on Cs/MMT, TiO_2 for 2 h under 180 min of irradiation, (c) Catalytic degradation of CBY3G-P by Cs/MMT nanocomposites for 2 h in the presence of ZnO, and (d) Photocatalytic degradation rate of CBY3G-P dye on Cs/MMT, ZnO for 2 h under 180 min of irradiation; Figure S2: (a) Catalytic degradation of CBY3G-P by Cs/MMT nanocomposites for 3 h in the presence of TiO_2, (b) Photocatalytic degradation rate of CBY3G-P dye on Cs/MMT, TiO_2 for 3 h under 180 min of irradiation, (c) Catalytic degradation of CBY3G-P by Cs/MMT nanocomposites for 3 h in the presence of ZnO, and (d) Photocatalytic degradation rate of CBY3G-P dye on Cs/MMT, ZnO for 3 h under 180 min of irradiation; Figure S3: (a) Catalytic degradation of CBY3G-P by Cs/MMT nanocomposites for 4 h in the presence of TiO_2, (b) Photocatalytic degradation rate of CBY3G-P dye on Cs/MMT, TiO_2 for 4 h under 180 min of irradiation, (c) Catalytic degradation of CBY3G-P by Cs/MMT nanocomposites for 4 h in the presence of ZnO, and (d) Photocatalytic degradation rate of CBY3G-P dye on Cs/MMT, ZnO for 4 h under 180 min of irradiation; Figure S4: (a) Catalytic degradation of CBY3G-P by Cs/MMT nanocomposites for 5 h in the presence of TiO_2, (b) Photocatalytic degradation rate of CBY3G-P dye on Cs/MMT, TiO_2 for 5 h under 180 min of irradiation, (c) Catalytic degradation of CBY3G-P by Cs/MMT nanocomposites for 5 h in the presence of ZnO, and (d) Photocatalytic degradation rate of CBY3G-P dye on Cs/MMT, ZnO for 5 h under 180 min of irradiation; Figure S5: (a) Catalytic degradation of CBY3G-P by Cs/HET nanocomposites for 1 h in the presence of TiO_2, (b) Photocatalytic degradation rate of CBY3G-P dye on Cs/HET, TiO_2 for 1 h under 180 min of irradiation, (c) Catalytic degradation of CBY3G-P by Cs/HET nanocomposites for 1 h in the presence of ZnO, and (d) Photocatalytic degradation rate of CBY3G-P dye on Cs/HET, ZnO for 1 h under 180 min of irradiation; Figure S6: (a) Catalytic degradation of CBY3G-P by Cs/HET nanocomposites for 2 h in the presence of TiO_2, (b) Photocatalytic degradation rate of CBY3G-P dye on Cs/HET, TiO_2 for 2 h under 180 min of irradiation, (c) Catalytic degradation of CBY3G-P by Cs/HET nanocomposites for 2 h in the presence of ZnO, and (d) Photocatalytic degradation rate of CBY3G-P dye on Cs/HET, ZnO for 2 h under 180 min of irradiation; Figure S7: (a) Catalytic degradation of CBY3G-P by Cs/HET nanocomposites for 3 h in the presence of TiO_2, (b) Photocatalytic degradation rate of CBY3G-P dye on Cs/HET, TiO_2 for 3 h under 180 min of irradiation, (c) Catalytic degradation of CBY3G-P by Cs/HET nanocomposites for 3 h in the presence of ZnO, and (d) Photocatalytic degradation rate of CBY3G-P dye on Cs/HET, ZnO for 3 h under 180 min of irradiation; Figure S8: (a) Catalytic degradation of CBY3G-P by Cs/HET nanocomposites for 4 h in the presence of TiO_2, (b) Photocatalytic degradation rate of CBY3G-P dye on Cs/HET, TiO_2 for 4 h under 180 min of irradiation, (c) Catalytic degradation of CBY3G-P by Cs/HET nanocomposites for 4 h in the presence of ZnO, and (d) Photocatalytic degradation rate of CBY3G-P dye on Cs/HET, ZnO4 h under 180 min of irradiation; Figure S9: (a) Catalytic degradation of CBY3G-P by Cs/HET nanocomposites for 5 h in the presence of TiO_2, (b) Photocatalytic degradation rate of CBY3G-P dye on Cs/HET, TiO_2 for 5 h under 180 min of irradiation, (c) Catalytic degradation of CBY3G-P by Cs/HET nanocomposites for 5 h in the presence of ZnO, and (d) Photocatalytic degradation rate of CBY3G-P dye on Cs/HET, ZnO for 5 h under 180 min of irradiation.

Conflicts of Interest: The authors declare no conflicts of interest.

References

1. Fatimah, I.; Wang, S.; Wulandari, D. ZnO/montmorillonite for photocatalytic and photochemical degradation of methylene blue. *Appl. Clay Sci.* **2011**, *53*, 553–560. [CrossRef]
2. Bahnemann, D. Photocatalytic water treatment: Solar energy applications. *Sol. Energy* **2004**, *77*, 445–459. [CrossRef]
3. Comninellis, C.; Kapalka, A.; Malato, S.; Parsons, S.A.; Poulios, I.; Mantzavinos, D. Advanced oxidation processes for water treatment: Advances and trends for R&D. *J. Chem. Technol. Biotechnol.* **2008**, *83*, 769–776. [CrossRef]
4. Goswami, D.; Vijayaraghavan, S.; Lu, S.; Tamm, G. New and emerging developments in solar energy. *Sol. Energy* **2004**, *76*, 33–43. [CrossRef]
5. Das, N.C.; Rahman, M.M.; Kabir, S.F. Preparation of novel clay/chitosan/ZnO bio-composite as an efficient adsorbent for tannery wastewater treatment. *Int. J. Biol. Macromol.* **2023**, *249*, 126136. [CrossRef]
6. Gupta, V.K.; Saravanan, R.; Agarwal, S.; Gracia, F.; Khan, M.M.; Qin, J.; Mangalaraja, R.V. Degradation of azo dyes under different wavelengths of UV light with chitosan-SnO$_2$ nanocomposites. *J. Mol. Liquids* **2017**, *232*, 423–430. [CrossRef]
7. Pomogailo, A.D.; Kestelman, V.N. Chemical methods of metal-polymer nanocomposite production. In *Metallopolymer Nanocomposites*; Springer: Berlin, Heidelberg, 2005; pp. 135–236. [CrossRef]
8. Aadnan, I.; Zegaoui, O.; Daou, I.; da Silva, J.C.E. Synthesis and physicochemical characterization of a ZnO-Chitosan hybrid-biocomposite used as an environmentally friendly photocatalyst under UV-A and visible light irradiations. *J. Environ. Chem. Eng.* **2020**, *8*, 104260. [CrossRef]
9. Ibhadon, A.O.; Fitzpatrick, P. Heterogeneous Photocatalysis: Recent Advances and Applications. *Catalysts* **2013**, *3*, 189–218. [CrossRef]
10. Li, H.; Wang, X.; Li, X.; Zhao, C.; Song, X.; Zhang, P.; Huo, P. A review on heterogeneous photocatalysis for environmental remediation: From semiconductors to modification strategies. *Chin. J. Catal.* **2022**, *43*, 178–214.
11. Wang, H.; Wan, Y.; Li, B.; Ye, J.; Gan, J.; Liu, J.; Huo, P. Rational design of Ce-doped CdS/N-rGO photocatalyst enhanced interfacial charges transfer for high effective degradation of tetracycline. *J. Mater. Sci. Technol.* **2024**, *173*, 137–148. [CrossRef]
12. Wang, B.; Zhang, R.; Li, Z.; Shi, C.; Liu, E.; Zheng, Z.; Zhou, B.; Ji, M.; Chen, H. Enhancing photocatalytic degradation efficiency via the construction of organic/inorganic S-scheme supramolecular hybrid heterostructures. *Appl. Surf. Sci.* **2023**, *641*, 158481. [CrossRef]
13. Aal, A.A.; Mahmoud, S.A.; Aboul-Gheit, A.K. Sol–Gel and Thermally Evaporated Nanostructured Thin ZnO Films for Photocatalytic Degradation of Trichlorophenol. *Nanoscale Res. Lett.* **2009**, *4*, 627–634. [CrossRef]
14. Schubnell, M.; Kamber, I.; Beaud, P. Photochemistry at high temperatures—Potential of ZnO as a high temperature photocatalyst. *Appl. Phys. A* **1997**, *64*, 109–113. [CrossRef]
15. Lahbib, M.; Meftah, M.; Mejri, C.; Oueslati, W.; Amara, A.B.H. The starting stoichiometry, keys parameter to enhance the intrinsic microstructural and functional properties of synthesized hybrid nanocomposites chitosan/Na-montmorillonite/ZnO nanoparticlest type. *Appl. Surf. Sci. Adv.* **2023**, *13*, 100369. [CrossRef]
16. Kango, S.; Kalia, S.; Celli, A.; Njuguna, J.; Habibi, Y.; Kumar, R. Surface modification of inorganic nanoparticles for development of organic–inorganic nanocomposites—A review. *Prog. Polym. Sci.* **2013**, *38*, 1232–1261. [CrossRef]
17. Wu, L.; Liao, L.; Lv, G. Influence of interlayer cations on organic intercalation of montmorillonite. *J. Colloid Interface Sci.* **2015**, *454*, 1–7. [CrossRef]
18. Hochella, M.F., Jr.; Mogk, D.W.; Ranville, J.; Allen, I.C.; Luther, G.W.; Marr, L.C.; McGrail, B.P.; Murayama, M.; Qafoku, N.P.; Rosso, K.M.; et al. Natural, incidental, and engineered nanomaterials and their impacts on the Earth system. *Science* **2019**, *363*, eaau8299. [CrossRef]
19. Putri, G.E.; Rilda, Y.; Syukri, S.; Labanni, A.; Arief, S. Enhancing morphological and optical properties of montmorillonite/chitosan-modified cerium oxide nanoparticles for antimicrobial applications. *Surf. Interfaces* **2022**, *32*, 102166. [CrossRef]
20. Giannakas, A.E.; Salmas, C.E.; Moschovas, D.; Baikousi, M.; Kollia, E.; Tsigkou, V.; Karakassides, A.; Leontiou, A.; Kehayias, G.; Avgeropoulos, A.; et al. Nanocomposite film development based on chitosan/polyvinyl alcohol using ZnO@ montmorillonite and ZnO@ halloysite hybrid nanostructures for active food packaging applications. *Nanomaterials* **2022**, *12*, 1843. [CrossRef]
21. Li, D.; Huang, X.; Hao, F.; Lv, Y.; Chen, H.; Wu, S.; Xiong, W.; Liu, P.; Luo, H. Preparation of organic-inorganic composites with high antibacterial activity based on sepiolite, chitosan and zinc: The study of the active antibacterial sites of chitosan-zinc oxide structure. *Appl. Clay Sci.* **2022**, *216*, 106325. [CrossRef]
22. Lee, D.-E.; Kim, M.-K.; Danish, M.; Jo, W.-K. State-of-the-art review on photocatalysis for efficient wastewater treatment: Attractive approach in photocatalyst design and parameters affecting the photocatalytic degradation. *Catal. Commun.* **2023**, *183*, 106764. [CrossRef]
23. Bagade, A.V.; Pund, S.N.; Nagwade, P.A.; Kumar, B.; Deshmukh, S.U.; Kanagare, A.B. Ni-doped Mg-Zn nano-ferrites: Fabrication, characterization, and visible-light-driven photocatalytic degradation of model textile dyes. *Catal. Commun.* **2023**, *181*, 106719. [CrossRef]
24. Ramirez, L.A.; Dennehy, M.; Alvarez, M. Metal oxide-biochar supported recyclable catalysts: A feasible solution for the reduction of 4-nitrophenol in water. *Catal. Commun.* **2023**, *181*, 106723. [CrossRef]

25. Bian, X.; Li, F.; Zhang, J.; Zhong, M.; Yang, Y.; Khan, S. Photocatalytic degradation of tetracycline antibiotics in swine wastewater using Fe^{3+}-loaded $NaBiO_3$ coupled with sodium persulfate. *Catal. Commun.* **2023**, *174*, 106579. [CrossRef]

26. Zehra, A.; Wani, S.M.; Bhat, T.A.; Jan, N.; Hussain, S.Z.; Naik, H.R. Preparation of a biodegradable chitosan packaging film based on zinc oxide, calcium chloride, nano clay and poly ethylene glycol incorporated with thyme oil for shelf-life prolongation of sweet cherry. *Int. J. Biol. Macromol.* **2022**, *217*, 572–582. [CrossRef]

27. Brahmi, M.; Essifi, K.; Bakirhan, N.K.; El Bachiri, A.; Ouldriane, S.D.; Tahani, A. New insights into physicochemical aspects involved in the formation of chitosan@ alginate biobased polyelectrolyte complexes on natural montmorillonite clay surface. *J. Mol. Liq.* **2023**, *387*, 122. [CrossRef]

28. Yahya, R.; Elshaarawy, R.F. Highly sulfonated chitosan-polyethersulfone mixed matrix membrane as an effective catalytic reactor for esterification of acetic acid. *Catal. Commun.* **2023**, *173*, 106557. [CrossRef]

29. Dutta, S.; Kumar, P.; Yadav, S.; Sharma, R.D.; Shivaprasad, P.; Vimaleswaran, K.S.; Srivastava, A.; Sharma, R.K. Accelerating innovations in CH activation/functionalization through intricately designed magnetic nanomaterials: From genesis to applicability in liquid/regio/photo catalysis. *Catal. Commun.* **2023**, *175*, 106615. [CrossRef]

30. Altıntıg, E.; Ates, A.; Angın, D.; Topal, Z.; Aydemir, Z. Kinetic, equilibrium, adsorption mechanisms of RBBR and MG dyes on chitosan-coated montmorillonite with an ecofriendly approach. *Chem. Eng. Res. Des.* **2022**, *188*, 287–300. [CrossRef]

31. Eltabey, R.M.; Abdelwahed, F.T.; Eldefrawy, M.M.; Elnagar, M.M. Fabrication of poly(maleic acid)-grafted cross-linked chitosan/montmorillonite nanospheres for ultra-high adsorption of anionic acid yellow-17 and cationic brilliant green dyes in single and binary systems. *J. Hazard. Mater.* **2022**, *439*, 129589. [CrossRef] [PubMed]

32. Tahari, N.; de Hoyos-Martinez, P.L.; Izaguirre, N.; Houwaida, N.; Abderrabba, M.; Ayadi, S.; Labidi, J. Preparation of chitosan/tannin and montmorillonite films as adsorbents for Methyl Orange dye removal. *Int. J. Biol. Macromol.* **2022**, *210*, 94–106. [CrossRef] [PubMed]

33. Wang, B.; Luo, C.-Y.; Zhu, P.; Liu, Y.; Xu, Y.-J. Facile construction of H_3PO_3-modified chitosan/montmorillonite coatings for highly efficient flame retardation of polyester–cotton fabrics. *Prog. Org. Coat.* **2023**, *184*, 107864. [CrossRef]

34. Albouchi, W.; Meftah, M.; Amara, A.B.H.; Oueslati, W. Effect of reactant ratio and nanofillers type on the microstructural properties, porosity fluctuations and heavy metal removal ability of chitosan-clay hybrid materials. *Appl. Surf. Sci. Adv.* **2023**, *13*, 100387. [CrossRef]

35. Franco, F.; Pozo, M.; Cecilia, J.A.; Benítez-Guerrero, M.; Lorente, M. Effectiveness of microwave assisted acid treatment on dioctahedral and trioctahedral smectites. The influence of octahedral composition. *Appl. Clay Sci.* **2016**, *120*, 70–80. [CrossRef]

36. Pálková, H.; Barlog, M.; Madejová, J.; Hronský, V.; Petra, L.; Šimon, E.; Billik, P.; Zimowska, M. Structural changes in smectites subjected to mechanochemical activation: The effect of the occupancy of the octahedral sites. *Appl. Clay Sci.* **2021**, *213*, 106214. [CrossRef]

37. Douillard, J.; Lantenois, S.; Prelot, B.; Zajac, J.; Henry, M. Study of the influence of location of substitutions on the surface energy of dioctahedral smectites. *J. Colloid Interface Sci.* **2008**, *325*, 275–281. [CrossRef] [PubMed]

38. Available online: https://www.clays.org/sourceclays_data/ (accessed on 29 March 2024).

39. Cheira, M.F.; Kouraim, M.N.; Zidan, I.H.; Mohamed, W.S.; Hassanein, T.F. Adsorption of U(VI) from sulfate solution using montmorillonite/polyamide and nano-titanium oxide/polyamide nanocomposites. *J. Environ. Chem. Eng.* **2020**, *8*, 104427. [CrossRef]

40. Mejri, C.; Oueslati, W.; Amara, A.B.H. Structure and reactivity assessment of dioctahedral montmorillonite during provoked variable sequential cation exchange process via XRD modelling approach. *Appl. Surf. Sci. Adv.* **2023**, *15*, 100403. [CrossRef]

41. Jiang, A.; Patel, R.; Padhan, B.; Palimkar, S.; Galgali, P.; Adhikari, A.; Varga, I.; Patel, M. Chitosan Based Biodegradable Composite for Antibacterial Food Packaging Application. *Polymers* **2023**, *15*, 2235. [CrossRef]

42. Biswal, A.; Sethy, P.K.; Swain, S.K. Change in orientation of polyacrylic acid and chitosan networks by imprintment of gold nanoparticles. *Polym. Technol. Mater.* **2020**, *60*, 182–194. [CrossRef]

43. Moll, W.F. Baseline studies of the clay minerals society source clays: Geological origin. *Clays Clay Miner.* **2001**, *49*, 374–380. [CrossRef]

44. Mermut, A.R.; Lagaly, G. Baseline studies of the clay minerals society source clays: Layer-charge determination and characteristics of those minerals containing 2:1 layers. *Clays Clay Miner.* **2001**, *49*, 393–397. [CrossRef]

45. Oueslati, W.; Meftah, M. Discretization of the water uptake process of Na-montmorillonite undergoing atmospheric stress: XRD modeling approach. *Adv. Mater. Sci. Eng.* **2018**, *2018*, 1–17. [CrossRef]

46. Ammar, M.; Oueslati, W.; Ben Rhaiem, H.; Amara, A.B.H. Effect of the hydration sequence orientation on the structural properties of Hg exchanged montmorillonite: Quantitative XRD analysis. *J. Environ. Chem. Eng.* **2014**, *2*, 1604–1611. [CrossRef]

47. Vinci, D.; Dazas, B.; Ferrage, E.; Lanson, M.; Magnin, V.; Findling, N.; Lanson, B. Influence of layer charge on hydration properties of synthetic octahedrally-charged Na-saturated trioctahedral swelling phyllosilicates. *Appl. Clay Sci.* **2019**, *184*, 105404. [CrossRef]

48. Fu, J.; Yang, F.; Guo, Z. The chitosan hydrogels: From structure to function. *New J. Chem.* **2018**, *42*, 17162–17180. [CrossRef]

49. Chipera, S.J.; Bish, D.L. Baseline studies of the clay minerals society source clays: Powder X-ray diffraction analyses. *Clays Clay Miner.* **2001**, *49*, 398–409. [CrossRef]

50. Borden, D.; Giese, R.F. Baseline studies of the clay minerals society source clays: Cation exchange capacity measurements by the ammonia-electrode method. *Clays Clay Miner.* **2001**, *49*, 444–445. [CrossRef]

51. Oueslati, W.; Ben Rhaiem, H.; Amara, A.B.H. Effect of relative humidity constraint on the metal exchanged montmorillonite performance: An XRD profile modeling approach. *Appl. Surf. Sci.* **2012**, *261*, 396–404. [CrossRef]

52. Oueslati, W.; Mejri, C.; Amara, A.B.H. Impact of uniaxial mechanical perturbation on structural properties and smectite porosity features: Ion exchanger efficiency and adsorption performance fate. *Adv. Civ. Eng.* **2022**, *2022*, 1–16. [CrossRef]

53. Jebali, S.; Meftah, M.; Mejri, C.; Ben Haj Amara, A.; Oueslati, W. Enhancement of Photocatalytic Activity and Microstructural Growth of Cobalt-Substituted Ba1−xCoxTiO$_3$ {x = 0,. . ., 1} Heterostructure. *ChemEngineering* **2023**, *7*, 43. [CrossRef]

54. Mejri, C.; Oueslati, W.; Amara, A.B.H. Structural alteration, hydration stability, heavy metal removal efficiency, and montmorillonite porosity fate by coupling the soil solution ph and a thermal gradient. *Adsorpt. Sci. Technol.* **2022**, *2022*, 1–28. [CrossRef]

55. Hussain, M.; Ceccarelli, R.; Marchisio, D.; Fino, D.; Russo, N.; Geobaldo, F. Synthesis, characterization, and photocatalytic application of novel TiO$_2$ nanoparticles. *Chem. Eng. J.* **2010**, *157*, 45–51. [CrossRef]

56. Shume, W.M.; Murthy, H.C.A.; Zereffa, E.A. A review on synthesis and characterization of Ag$_2$O nanoparticles for photocatalytic applications. *J. Chem.* **2020**, *2020*, 1–15. [CrossRef]

57. Kefeni, K.K.; Mamba, B.B. Photocatalytic application of spinel ferrite nanoparticles and nanocomposites in wastewater treatment: Review. *Sustain. Mater. Technol.* **2020**, *23*, e00140. [CrossRef]

58. Bhattacharjee, M.; Goswami, S.; Pramanik, N.B.; Barman, J.; Saikia, M.; Hulle, N.R.S.; Haloi, D.J. Chitosan/Clay biocomposite films with enhanced physico-chemical, mechanical and antimicrobial properties. *Anal. Chem. Lett.* **2023**, *13*, 609–625. [CrossRef]

59. Vijayalekshmi, V. UV-Visible, mechanical and anti-microbial studies of chitosan-montmorillonite clay/TiO$_2$ nanocomposites. *Res. J. Recent Sci.* **2015**, *4*, 131–135.

60. Bahrudin, N.N.; Nawi, M.A.; Zainal, Z. Insight into the synergistic photocatalytic-adsorptive removal of methyl orange dye using TiO$_2$/chitosan based photocatalyst. *Int. J. Biol. Macromol.* **2020**, *165*, 2462–2474. [CrossRef]

61. Gao, X.; Yin, H.; Li, M.; Xin, L.; Zhang, H.; Long, H. Photocatalytic degradation of methyl orange by a diethylenetriamine modified chitosan/bentonite composite. *React. Chem. Eng.* **2023**, *8*, 2505–2521. [CrossRef]

62. Bahrudin, N.N.; Nawi, M.A.; Sabar, S. Immobilized chitosan-montmorillonite composite adsorbent and its photocatalytic regeneration for the removal of methyl orange. *React. Kinet. Catal. Lett.* **2019**, *126*, 1135–1153. [CrossRef]

63. Aadnan, I.; Zegaoui, O.; El Mragui, A.; Esteves da Silva, J.C.G. Physicochemical and photocatalytic properties under visible light of ZnO-Bentonite/Chitosan hybrid-biocompositefor water remediation. *Nanomaterials* **2021**, *12*, 102. [CrossRef]

64. Bai, Q.; Yangchao, L. A review on the preparation and characterization of chitosan-clay nanocomposite films and coatings for food packaging applications. *Carbohydr. Polym. Technol. Appl.* **2021**, *2*, 100102.

65. Butman, M.F.; Ovchinnikov, N.L.; Karasev, N.S.; Kochkina, N.E.; Agafonov, A.V.; Vinogradov, A.V. Photocatalytic and adsorption properties of TiO$_2$-pillared montmorillonite obtained by hydrothermally activated intercalation of titanium polyhydroxo complexes. *Beilstein J. Nanotechnol.* **2018**, *9*, 364–378. [CrossRef]

66. Huo, M.; Guo, H.; Jiang, Y.; Ju, H.; Xue, B.; Li, F. A facile method of preparing sandwich layered TiO$_2$ in between montmorillonite sheets and its enhanced UV-light photocatalytic activity. *J. Photochem. Photobiol. A Chem.* **2018**, *358*, 121–129. [CrossRef]

67. Amir, M.N.I.; Julkapli, N.M.; Hamid, S.B.A. Incorporation of chitosan and glass substrate for improvement in adsorption, separation, and stability of TiO$_2$ photodegradation. *Int. J. Environ. Sci. Technol.* **2016**, *13*, 865–874. [CrossRef]

68. Saravanan, R.; Aviles, J.; Gracia, F.; Mosquera, E.; Gupta, V.K. Crystallinity and lowering band gap induced visible light photocatalytic activity of TiO$_2$/CS (Chitosan) nanocomposites. *Int. J. Biol. Macromol.* **2018**, *109*, 1239–1245. [CrossRef]

69. Cesur, S.; Köroğlu, C.; Yalçın, H.T. Antimicrobial and biodegradable food packaging applications of polycaprolactone/organo nanoclay/chitosan polymeric composite films. *J. Vinyl Addit. Technol.* **2018**, *24*, 376–387. [CrossRef]

70. Mohammadzadeh-Vazifeh, M.; Hosseini, S.M.; Mohammadi, A.; Jahanfar, M.; Maleki, H. Investigation of the antimicrobial properties of nanoclay and chitosan based nanocomposite on the microbial characteristics of Gouda cheese. *Iran. J. Microbiol.* **2020**, *12*, 121–126. [CrossRef]

71. Kusmono; Abdurrahim, I. Water sorption, antimicrobial activity, and thermal and mechanical properties of chitosan/clay/glycerol nanocomposite films. *Heliyon* **2019**, *5*, e02342. [CrossRef]

72. Khubiev, O.M.; Egorov, A.R.; Kirichuk, A.A.; Khrustalev, V.N.; Tskhovrebov, A.G.; Kritchenkov, A.S. Chitosan-Based Antibacterial Films for Biomedical and Food Applications. *Int. J. Mol. Sci.* **2023**, *24*, 10738. [CrossRef]

73. Priyadarshi, R.; Rhim, J.-W. Chitosan-based biodegradable functional films for food packaging applications. *Innov. Food Sci. Emerg. Technol.* **2020**, *62*, 102346. [CrossRef]

74. Ben Dhieb, F.; Dil, E.J.; Tabatabaei, S.H.; Mighri, F.; Ajji, A. Effect of nanoclay orientation on oxygen barrier properties of LbL nanocomposite coated films. *RSC Adv.* **2019**, *9*, 1632–1641. [CrossRef]

75. Kumar, S.; Mukherjee, A.; Dutta, J. Chitosan based nanocomposite films and coatings: Emerging antimicrobial food packaging alternatives. *Trends Food Sci. Technol.* **2020**, *97*, 196–209. [CrossRef]

76. Cankaya, N.; Sahin, R. Chitosan/clay bionanocomposites: Structural, antibacterial, thermal and swelling properties. *Cellul. Chem. Technol.* **2019**, *53*, 537–549. [CrossRef]

77. Bandyopadhyay, J.; Ray, S.S. Are nanoclay-containing polymer composites safe for food packaging applications?—An overview. *J. Appl. Polym. Sci.* **2019**, *136*, 47214. [CrossRef]

78. Rodrigues, C.; de Mello, J.M.M.; Dalcanton, F.; Macuvele, D.L.P.; Padoin, N.; Fiori, M.A.; Soares, C.; Riella, H.G. Mechanical, thermal and antimicrobial properties of chitosan-based-nanocomposite with potential applications for food packaging. *J. Polym. Environ.* **2020**, *28*, 1216–1236. [CrossRef]

79. El-Naggar, E.; Wassel, M.A.; Shoueir, R.K. Visible-light driven photocatalytic effectiveness for solid-state synthesis of ZnO/natural clay/TiO$_2$ nanoarchitectures towards complete decolorization of methylene blue from aqueous solution. *Environ. Nanotechnol. Monit. Manag.* **2021**, *15*, 100425. [CrossRef]

80. Mustapha, S.; Ndamitso, M.M.; Abdulkareem, A.S.; Tijani, J.O.; Shuaib, D.T.; Ajala, A.O.; Mohammed, A.K. Application of TiO$_2$ and ZnO nanoparticles immobilized on clay in wastewater treatment: A review. *Appl. Water Sci.* **2020**, *10*, 49. [CrossRef]

81. Jida, S.M.; Zerefa, E.A. Preparation and photocatalysis of ZnO/bentonite based on adsorption and photocatalytic activity. *Mater. Res. Express* **2023**, *10*, 035502. [CrossRef]

82. Morlando, A.; Sencadas, V.; Cardillo, D.; Konstantinov, K. Suppression of the photocatalytic activity of TiO$_2$ nanoparticles encapsulated by chitosan through a spray-drying method with potential for use in sunblocking applications. *Powder Technol.* **2018**, *329*, 252–259. [CrossRef]

83. Castillo, P.C.H.-D.; Castro-Velázquez, V.; Rodríguez-González, V. Adsorption and photocatalytic-conjugated activity of a chitosan-functionalized titanate coating for the removal of the drug clonazepam from drinking water. *Environ. Sci. Pollut. Res.* **2023**, 1–16. [CrossRef]

84. Maruthupandy, M.; Muneeswaran, T.; Chackaravarthi, G.; Vennila, T.; Anand, M.; Cho, W.-S.; Quero, F. Synthesis of chitosan/SnO$_2$ nanocomposites by chemical precipitation for enhanced visible light photocatalytic degradation efficiency of congo red and rhodamine-B dye molecules. *J. Photochem. Photobiol. A Chem.* **2022**, *430*, 113972. [CrossRef]